Room-Temperature Sputtered SnO2-Based Thin Films as Earth-Abundant Transparent Conductive Oxides for Photovoltaic Applications

Saitta, F.S.; Padmakumar, G.; Perez Rodriguez, P.; Wilson, A.T.; Gonugunta, P.; Ravi Anusuyadevi, P.; Santbergen, R.; Smets, A.H.M.

DOI
10.1021/acsaelm.5c01650

Publication date
2025

Document Version
Final published version

Published in
ACS Applied Electronic Materials

ACS APPLIED ELECTRONIC MATERIALS

pubs.acs.org/acsaelm

Article

Room-Temperature Sputtered SnO_2-Based Thin Films as Earth-Abundant Transparent Conductive Oxides for Photovoltaic Applications

Federica Saitta,* Govind Padmakumar, Paula Perez Rodriguez, Alestair Wilson, Prasad Gonugunta, Prasaanth Ravi Anusuyadevi, Rudi Santbergen, and Arno H.M. Smets

Cite This: ACS Appl. Electron. Mater. 2025, 7, 9489−9504

Read Online

ACCESS | Metrics & More | Article Recommendations | Supporting Information

ABSTRACT: This study investigates the influence of reactive sputtering gas composition, specifically the oxygen-to-argon (O_2/Ar) and hydrogen-to-argon (H_2/Ar) ratios, on the optoelectrical and structural properties of fluorine-doped tin oxide (FTO) and undoped tin dioxide (SnO_2) thin films deposited at room temperature (RT). Through systematic variation of O_2 and H_2 content in the sputtering atmosphere, gas-phase composition is correlated with key performance metrics, including optical transmittance, sheet resistance, carrier density, and mobility, both before and after postdeposition annealing (PDA) at 400 °C in a nitrogen atmosphere. An optimal O_2/Ar ratio of 0.3−0.4% achieves the best optoelectrical trade-off in FTO, yielding a minimum sheet resistance (468 Ω/sq) and high mobility (13.7 $cm^2/(V\,s)$). In SnO_2 films, increasing oxygen improves optical transparency but reduces conductivity, while hydrogen incorporation at fixed 1% O_2/Ar enhances transparency and lowers sheet resistance in the as deposited state. These effects are attributed to defect passivation rather than changes in oxidation state, as supported by X-ray photoelectron spectroscopy results. Ambipolar conduction observed in the as deposited films transitions to stable n-type behavior after PDA, highlighting the role of thermal treatment. Although RT sputtered SnO_2-based films do not yet match the performance of high-temperature grown benchmarks, these findings demonstrate that careful tuning of the sputtering gas composition enables scalable, thermally compatible, and cost-effective fabrication of transparent conducting electrodes and transport layers in photovoltaic applications.

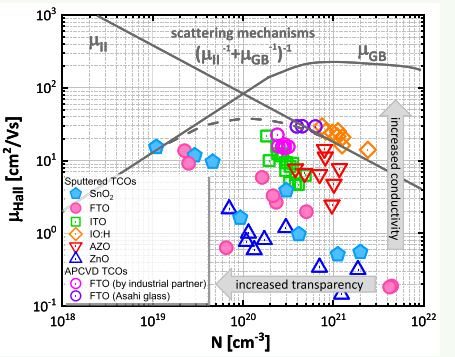

KEYWORDS: *tin dioxide (SnO_2), fluorine-doped tin oxide (FTO), room-temperature processing, reactive gas composition, ambipolar charge carrier density, photovoltaic applications*

1. INTRODUCTION

Transparent conducting oxides (TCOs) are critical components in modern optoelectronic devices due to their unique combination of high optical transmittance and electrical conductivity. Indium tin oxide (ITO) remains the benchmark due to its optimal trade-off between optical and electrical performance. However, its reliance on scarce and costly indium, along with sustainability concerns, motivates the search for earth-abundant, indium-free alternatives.[1] Among these, tin-based compounds such as undoped tin dioxide (SnO_2) and fluorine-doped tin oxide (SnO_2:F or FTO) have attracted growing interest as promising candidates to replace ITO in these technologies.[2,3]

Fluorine-doped tin oxide is widely employed in industry when deposited at elevated temperatures (∼500 °C), typically via atmospheric pressure chemical vapor deposition (APCVD), as exemplified by commercially available Asahi glass substrates.[4] This choice is primarily driven by the excellent crystallinity and superior carrier transport properties of FTO, which are crucial for photovoltaic and other optoelectronic applications.[5,6] However, such high-temperature processes are incompatible with many emerging applications that require temperature-sensitive substrates, such as flexible photovoltaics (e.g., on PEN or PET), tandem solar cells, and roll-to-roll and printing-based manufacturing.[7,8]

Room-temperature (RT) sputtering offers a low-thermal-budget route to TCOs with large-area uniformity and scalability. RT sputtered SnO_2 has been employed as an electron transport layer (ETL) in perovskite solar cells, delivering efficiencies above 17% with extended operational lifetimes and compatibility with flexible substrates.[9,10] This approach also enables sequential layer-by-layer processing, essential for tandem architectures where subcells are fabricated

Received: August 8, 2025
Revised: September 24, 2025
Accepted: September 26, 2025
Published: October 9, 2025

under strict thermal constraints.[11] Moreover, amorphous SnO_2 deposited at RT has improved electrical contact properties in indium-free silicon heterojunction (SHJ) solar cells without sacrificing efficiency.[12,13]

Although RT deposition of SnO_2 films offers significant advantages for flexible and temperature-sensitive device integration, it typically results in films with limited crystallinity, incomplete dopant activation, and suboptimal electrical performance. Therefore, postdeposition annealing (PDA) treatments at moderate temperatures have proven effective in improving the structural and electronic properties of RT-deposited films without exceeding the thermal budgets of sensitive substrates or adjacent layers.[14−16] Furthermore, annealing in reducing atmospheres can further optimize carrier transport and electrical performance of SnO_2 thin films.[17]

While achieving high optoelectrical performance in RT-deposited SnO_2 and FTO remains challenging, the potential of sputtering gas composition to tailor these properties has not been sufficiently explored for photovoltaic applications. In particular, the combined effects of oxygen, critical for stoichiometry and bandgap control, and hydrogen, known to influence carrier generation, defect chemistry, and passivation, have not been systematically studied in SnO_2-based films under RT sputtering conditions.[18−21]

To address this gap in understanding, this study investigates the effect of varying oxygen and hydrogen gas ratios during sputtering on the optoelectrical properties of RT-deposited SnO_2-based films. A postdeposition thermal treatment at 400 °C in nitrogen is applied to assess whether optimized gas-phase deposition conditions can reproduce, in part or in full, the optoelectrical improvements typically obtained through annealing.

This investigation therefore focuses on key optoelectrical metrics relevant to the integration of TCOs in photovoltaic devices, specifically as front electrodes or electron transport layers, including optical transmittance, bandgap energy, carrier density, mobility, and sheet resistance. By correlating these properties with compositional and structural analyses, this work evaluates whether optimized RT-deposited films can approach the performance of their commercial high-temperature SnO_2-based counterparts, offering a pathway toward scalable, cost-effective, and thermally compatible solutions for next-generation photovoltaic technologies.

2. EXPERIMENTAL PROCEDURE

This section describes the preparation and characterization of FTO and SnO_2 thin films. Section 2.1 details the deposition parameters and gas environments used during the RF magnetron sputtering of the films. Section 2.2 explains the postdeposition annealing process. Section 2.3 presents the optical and electrical characterization methods, and Section 2.4 focuses on structural and compositional material analyses.

2.1. Film Deposition. Fluorine-doped tin oxide (FTO) and undoped tin oxide (SnO_2) thin films are deposited onto Corning Eagle 2000 glass substrates using the radio frequency (RF, 13.56 MHz) magnetron sputtering technique. The substrates, which have dimensions of 10 cm × 2.5 cm × 0.7 mm, are subjected to ultrasonic cleaning in acetone and isopropyl alcohol for 10 min each to remove contaminants before deposition.

Ceramic targets supplied by Process Materials Inc. are utilized in the deposition process, including a SnO_2 target of 99.99% purity for SnO_2 films and a target of 98 wt % SnO_2 with 2 wt % SnF_2, also at 99.99% purity, for FTO films. The sputtering process occurs at room temperature, with a substrate temperature of approximately 19 °C, in a high-vacuum chamber with a base pressure of 1×10^{-6} mbar. Prior to deposition, a 5 min presputtering step is performed to clean the target surface.

Two distinct batches of experiments are conducted to investigate the effect of reactive gas composition on film properties. In the first batch, the oxygen-to-argon (O_2/Ar) ratio is varied from 0% to 0.4% for FTO films and from 0% to 1% for SnO_2 films, with 0% O_2/Ar corresponding to sputtering in a pure argon atmosphere. In the second batch, the O_2/Ar ratio is fixed at 1% for both materials, while the hydrogen-to-argon (H_2/Ar) ratio is varied from 0% to 0.6%. Here, 0% H_2/Ar refers to the baseline oxygen condition (1% O_2/Ar) with no hydrogen added.

All films are deposited at a constant working pressure of 6×10^{-3} mbar. The total gas flow rate remains constant at 50 sccm, using pure argon along with controlled mixtures of oxygen (up to 1% O_2 in Ar) and hydrogen (up to 0.6% H_2 in Ar). All films are deposited at a rate of 0.04 nm/s using an RF power density at 0.8 W/cm^2.

2.2. Postdeposition Annealing. Following deposition, the films undergo postdeposition annealing (PDA) to assess its effect on their optoelectrical properties. Annealing is carried out at 400 °C for 20 min in a pure nitrogen (N_2) atmosphere using a Solaris rapid thermal processing (RTP) system, which provides rapid heating and cooling with precise temperature control and a heating rate of 10 °C/s.

2.3. Optical and Electrical Characterization. The transmittance (T) and reflectance (R) spectra of the deposited films are measured using a PerkinElmer Lambda 1050 spectrophotometer. The characterization is conducted over the spectral range of 300−1200 nm, covering the relevant portion of the solar spectrum where efficient light transmission is essential for FTO and SnO_2 in their role as front electrodes in solar cell applications.

The optical bandgap energy (E_g) is extracted using the Tauc plot method.[22] The absorption coefficient (α) is first calculated from transmittance and reflectance data using the relation $\alpha(\lambda) = (1/t) \ln[(100 - R_{\%}(\lambda))/T_{\%}(\lambda)]$, where t is the film thickness.

For direct bandgap materials such as SnO_2 and FTO, the optical bandgap (E_g) is determined by plotting $(\alpha h\nu)^2$ against photon energy ($h\nu$), following the relation $(\alpha h\nu)^2 = A(h\nu - E_g)$, where A is a proportionality constant and $h\nu$ represents the photon energy. The bandgap value is determined by extending the linear portion of the curve to the energy axis, corresponding to zero absorption Additional details are provided in the Supporting Information.

To complement the bandgap analysis and gain insight into defect-related states, the absorption edge is further examined using the Urbach rule. In this model, the absorption coefficient follows an exponential dependence on photon energy in the sub-bandgap region, expressed as $\alpha(h\nu) = \alpha_0 \exp(h\nu/E_e)$, where α_0 is a constant and E_e is the Urbach energy.[23] This parameter quantifies the width of the exponential tail, which reflects structural disorder and the presence of localized states within the bandgap.[24,25] Values of E_e are obtained from the slope of $\ln(\alpha)$ versus the photon energy in the low-energy region. Further details are provided in the Supporting Information.

The film thickness is determined using a Steag ETA-Optik mini-RT setup. In mini-RT measurements, R and T spectra are recorded and processed through Scout software to estimate the sample thickness.

The sheet resistance (R_{sh}) is measured by using the four-point probe (4PP) method with an AIT CMT-SR2000N measurement system. In this configuration, four equidistant probes are arranged in a linear geometry to ensure consistent and accurate readings.

The resistivity (ρ) is measured using an HMS-5000 Hall Effect measurement system via the van der Pauw method. The carrier density (N) and mobility (μ) are derived from Hall effect measurements at room temperature. The magnetic flux density is set to 0.55 T, and the input current is 10 mA. The probes are arranged in a square configuration with approximately 1 cm spacing, ensuring uniform geometry for accurate measurements. The sample thickness is determined beforehand using the mini-RT setup.

2.3.1. Hall Effect and Carrier Transport Measurements. Hall effect measurements on SnO_2-based materials, including fluorine-doped tin oxide (FTO), present inherent challenges, particularly when evaluating intrinsic or near-intrinsic films. In undoped SnO_2, the conduction arises primarily from thermally excited carriers or native

https://doi.org/10.1021/acsaelm.5c01650
ACS Appl. Electron. Mater. 2025, 7, 9489−9504

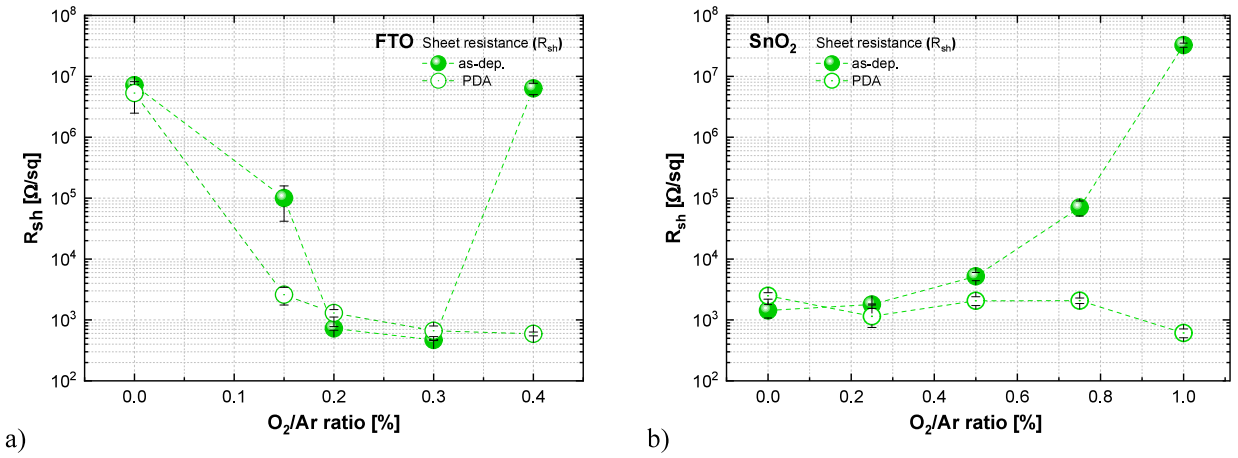

Figure 1. Sheet resistance (R_{sh}) of (a) FTO and (b) SnO_2 films as a function of the O_2/Ar ratio in as deposited (as-dep.) and postdeposition annealed (PDA) conditions.

defects, leading to mixed conduction.[26,27] In this regime, both electrons and holes contribute to transport, and the Hall coefficient (R_H) is governed by their respective concentrations and mobilities:[28]

$$R_H = \frac{p\mu_h^2 - n\mu_e^2}{q(n\mu_e + p\mu_h)^2}$$

where p and μ_h are the hole concentration and mobility, respectively; n and μ_e are the electron concentration and mobility, respectively; and q is the elementary charge.

The formula can be simplified for intrinsic materials ($n \approx p$) as

$$R_H = \frac{\mu_h^2 - \mu_e^2}{qn(\mu_e + \mu_h)^2}$$

This highlights that the sign and magnitude of the Hall coefficient reflect not just carrier type but also relative mobilities. It means that intrinsic SnO_2-based films can appear as n-type due to the higher mobility of electrons or as p-type due to the higher mobility of holes.

Note the excitation current is set to 10 mA in this study. Although lower excitation currents (<1 mA) are commonly used for high-resistivity materials to limit Joule heating, a higher current is employed in this study to improve the signal-to-noise ratio and enable the reliable detection of Hall voltages. To ensure comparability across all samples, the measurement configuration, including current, magnetic field strength, and contact geometry, is kept constant. This consistency is critical when evaluating carrier concentration and mobility across SnO_2-based and other transparent conducting oxide films.

Each Hall measurement is repeated five times, and the reported carrier concentrations and mobilities represent average values. The standard deviation from these repetitions is reported as the measurement uncertainty. In this study, both positive and negative Hall coefficients are observed across different samples. However, for each individual sample, the sign of the Hall voltage remained consistent across all five measurements.

2.3.2. Optoelectrical Metrics. The optoelectrical characterization of SnO_2-based films is guided by their intended function as either front electrodes or electron transport layers in solar cell applications.[29,30] The selected metrics provide a comprehensive understanding of the trade-offs between optical transparency and electrical conductivity.

For front-contact applications, high optical transmittance across the solar spectrum is essential to maximize photon flux reaching the active layer of solar devices. Minimal reflectance and a wide bandgap help suppress parasitic absorption in the ultraviolet (UV) and visible region, particularly in the blue portion of the spectrum where band-to-band absorption may occur.

However, according to the Drude model,[31] increased carrier concentration enhances free carrier absorption (FCA) in the near-infrared (NIR) region, which can degrade optical transparency in this range. Therefore, while a certain level of doping is necessary to improve conductivity, excessive carrier density leads to undesirable absorption losses.

Electrically, the TCO must exhibit low sheet resistance to enable efficient lateral charge transport toward metal contacts when functioning as a front electrode or from the perovskite absorber to the electrode when serving as an ETL. Achieving high Hall mobility is also crucial: it facilitates effective carrier transport and mitigates FCA by reducing carrier scattering.

2.4. Structural and Compositional Characterization. To support and explain trends observed in the optoelectrical properties of the SnO_2-based films, a comprehensive material characterization is conducted, focusing on the bulk composition, crystallinity, and surface chemistry.

Energy dispersive X-ray spectroscopy (EDX) is employed to confirm the presence and relative atomic percentages of Sn, O, and F in the bulk of the films. The measurements are carried out on samples deposited on (100)-oriented silicon wafers to minimize substrate interference, using a Nova NanoSEM 650 instrument equipped with an integrated EDX detector operating at 15 kV. Quantification is performed using the eZAF Smart Quant algorithm, and the atomic percentages along with relative uncertainties are reported in the Supporting Information.

X-ray photoelectron spectroscopy (XPS) is performed to analyze the surface chemistry and oxidation states of the constituent elements. Measurements are carried out using a PHI 5400 ESCA system (Physical Electronics, Inc.) equipped with a nonmonochromatized Al Kα X-ray source (hv = 1486.7 eV), operating at 200 W with an accelerating voltage of 13.5 kV. The takeoff angle is fixed at 45° for both survey and high-resolution scans. Each measurement covers a circular analysis area that is 0.4 mm in diameter with an effective sampling depth of approximately 3−5 nm. All XPS spectral processing is performed using MultiPak version 8.0 (Physical Electronics, Inc.). A Shirley-type background subtraction is applied to curve fitting. For the analysis of high-resolution XPS data, the charge neutralization is performed by referencing the C−C peak of the C 1s spectrum at 284.4 eV prior to curve fitting.

The crystalline structure of the films is analyzed using X-ray diffraction (XRD). Diffraction patterns are acquired with a Bruker D8 Advance diffractometer configured in Bragg−Brentano geometry, using Cu Kα radiation (λ = 1.5406 Å). The X-ray tube operates with a standard focus, providing sufficient intensity for high-resolution phase identification.

The surface and cross-sectional morphologies of the films are investigated using field-emission scanning electron microscopy (FE-SEM). A Hitachi Regulus 8230 system is used to obtain high-

https://doi.org/10.1021/acsaelm.5c01650
ACS Appl. Electron. Mater. 2025, 7, 9489−9504

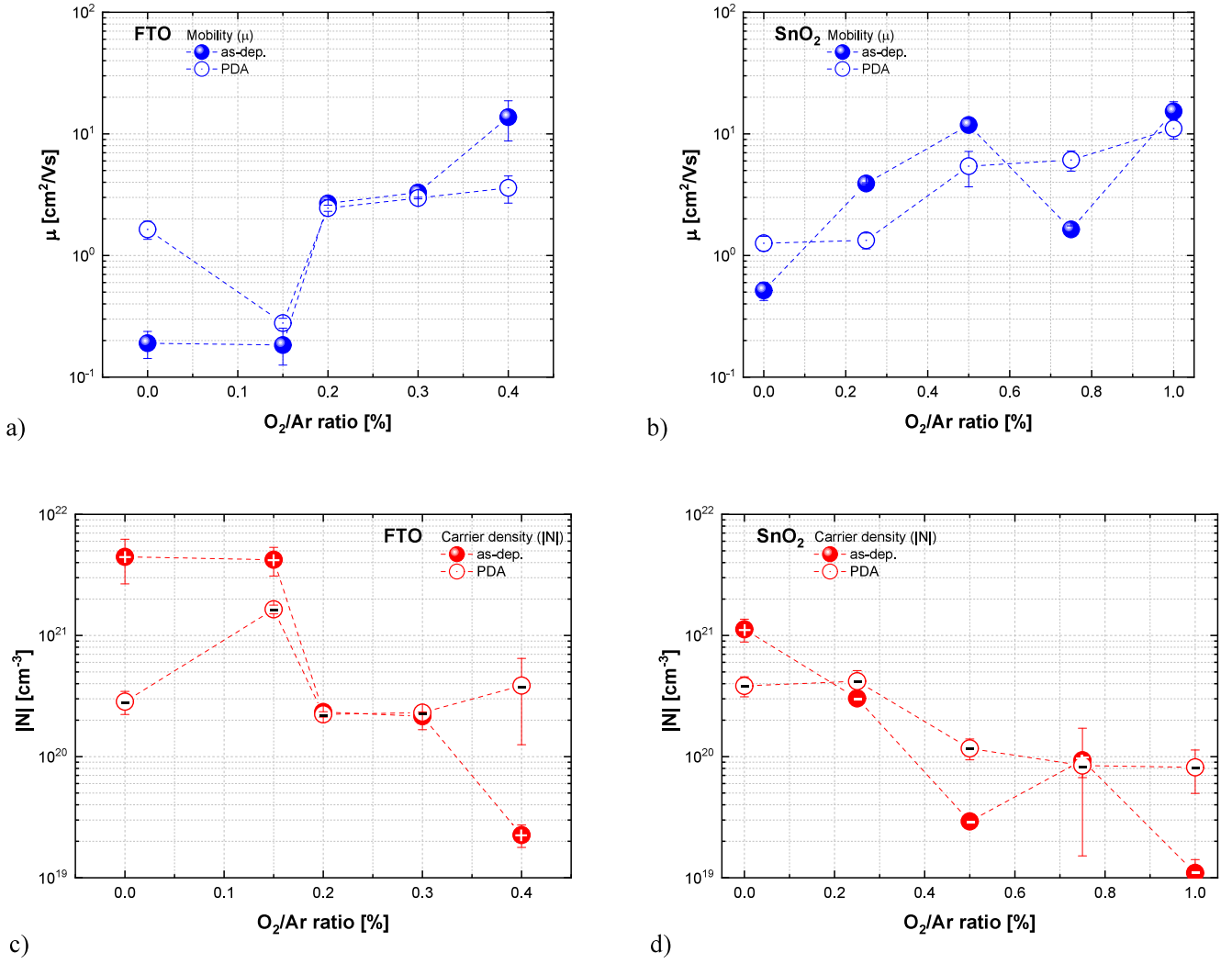

Figure 2. Carrier mobility (μ) and density (N) of (a, c) FTO and (b, d) SnO_2 films as a function of the O_2/Ar ratio in as deposited (as-dep.) and postdeposition annealed (PDA) conditions. The carrier density sign is reported on the red dots.

resolution images and evaluate surface texture, film growth, and structure. SEM images are included in the Supporting Information.

3. RESULTS AND DISCUSSION

The study first examines the optoelectronic properties of FTO and SnO_2 films. The effects of varying the O_2/Ar and H_2/Ar ratios are analyzed in Sections 3.1.1 and 3.1.2, respectively. In Section 3.2, the material properties are studied through energy dispersive X-ray spectroscopy (EDX) , X-ray photoelectron spectroscopy (XPS), and X-ray diffraction (XRD). The role of postdeposition annealing (PDA) is also evaluated, and all measurements are performed on approximately 200 nm thick films.

3.1. Optoelectrical Properties. *3.1.1. Oxygen Series.* To assess the impact of oxygen on the optoelectrical properties of FTO and SnO_2 films, the sheet resistance is used as a key performance metric due to its direct correlation with electrical conductivity in transparent electrodes. In photovoltaic devices, the R_{sh} of the TCO layer contributes to the total series resistance (R_s) of the device. A high R_{sh} increases voltage drops during lateral charge collection, leading to power losses and a reduced fill factor. Therefore, minimizing R_{sh} is essential for ensuring efficient charge transport toward the metal contact, preserving high current extraction and overall device performance.

Figure 1 shows the sheet resistance trends of both FTO and SnO_2 films as a function of increasing O_2/Ar ratio in the sputtering atmosphere. For the 0% O_2/Ar condition, the films are deposited in a pure argon environment, serving as the baseline reference.

In FTO (Figure 1a), the sheet resistance follows a U-shaped trend, reaching its minimum value of 468 Ω/sq at 0.3% O_2/Ar, before increasing sharply at an O_2/Ar ratio ≥0.4%. Oxygen levels between 0.4% and 1% O_2/Ar result in R_{sh} values exceeding 10^7 Ω/sq, which are far above the threshold relevant for low-thermal-budget solar cell applications. These conditions are therefore excluded from the investigation.

For the SnO_2 films (Figure 1b), the O_2/Ar ratio is extended to 1%, corresponding to the upper limit of the sputtering system. The R_{sh} exhibits an exponential-like increase with increasing oxygen content, indicating a continuous degradation in electrical conductivity across the investigated range. The minimum R_{sh} value of 610 Ω/sq is achieved at 1% O_2/Ar after thermal treatment.

Overall, the postdeposition annealing induces a consistent downward shift in sheet resistance toward approximately 10^3

https://doi.org/10.1021/acsaelm.5c01650
ACS Appl. Electron. Mater. 2025, 7, 9489−9504

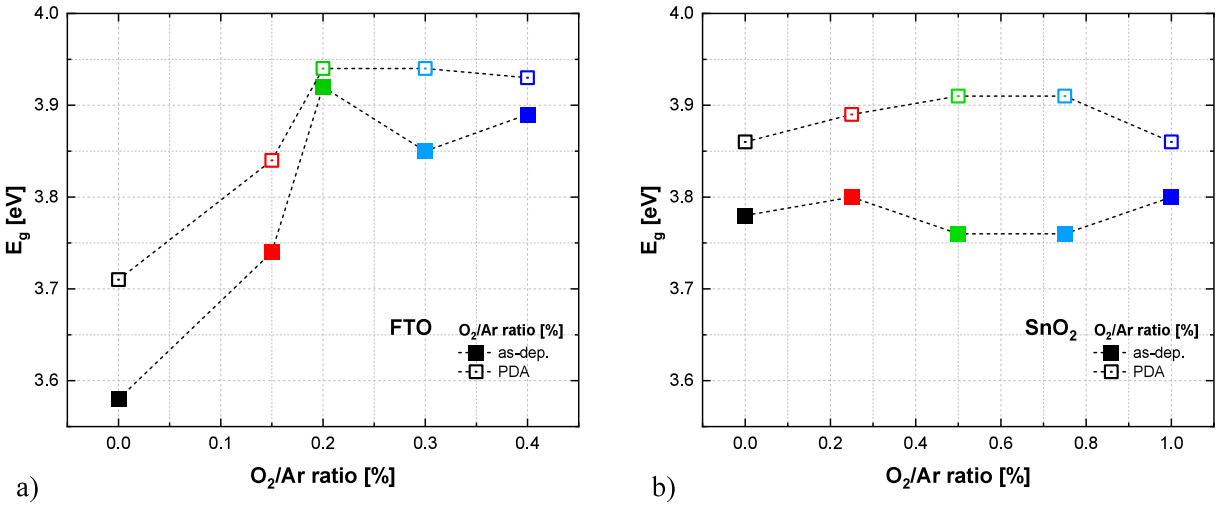

Figure 3. Optical bandgap (E_g) of (a) FTO and (b) SnO_2 films as a function of the O_2/Ar ratio in as deposited (as-dep.) and postdeposition annealed (PDA) conditions.

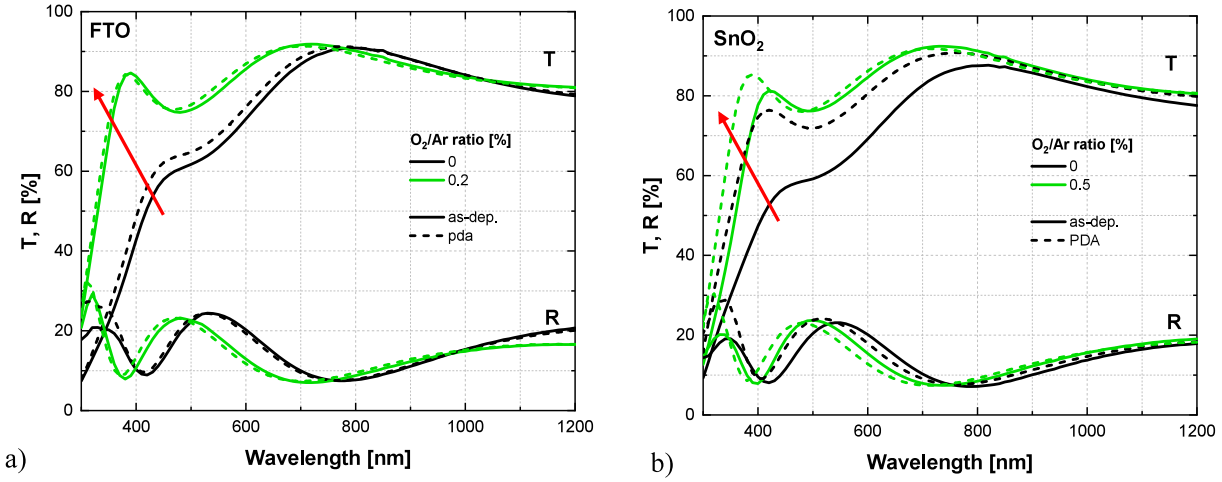

Figure 4. Transmittance (T) and reflectance (R) spectra of (a) FTO and (b) SnO_2 films (~200 nm thick) in as deposited (as-dep.) and postdeposition annealed (PDA) states. The films are sputtered in oxygen-deficient and oxygen-containing atmospheres.

Ω/sq for both materials, even when the oxygen content initially causes a significant reduction in conductivity.

Figure 2 illustrates the evolution of μ and N in the FTO and SnO_2 films as a function of the O_2/Ar ratio under both as deposited and PDA conditions. A general trend is observed where increasing oxygen content in the sputtering atmosphere leads to higher mobility and lower carrier density in both processing states.

In the FTO films (Figure 2a,c), the highest mobility (13.73 $cm^2/(V\ s)$) and lowest carrier density (2.25×10^{19} cm^{-3}) are achieved at 0.4% O_2/Ar in the as deposited films. In comparison, the SnO_2 films (Figure 2b,d) exhibit slightly better values, with the highest mobility (15.34 $cm^2/(V\ s)$) and lowest carrier density (1.10×10^{19} cm^{-3}) obtained at 1% O_2/Ar.

Hall effect measurements revealed both positive and negative Hall coefficients in the FTO and SnO_2 films, suggesting an apparent ambipolar behavior. Because Hall analysis in mixed conduction systems is inherently ambiguous, no definitive conclusion can be drawn on the conduction type from these data alone. Accordingly, the discussion emphasizes relative differences and overall trends rather than absolute values. Further details on the measurement procedure are provided in Section 2.3.1. Discussion of the ambipolar behavior is given in Section 3.1.3, and complete N values are listed in the Supporting Information.

Despite the high Hall mobility and low carrier concentration at 0.4% O_2/Ar, the four-point probe measured sheet resistance is comparatively high. This difference arises because Hall and four-point probe measurements independently assess the carrier transport and overall resistance, respectively. Thus, favorable Hall parameters do not always correspond to low sheet resistance, highlighting the need to report both for a complete electrical characterization.[32−34]

The values reported here are in good agreement with those of previous studies on TCO films deposited at or near room temperature. Banyamin et al.[39] reported mobility values around 15 $cm^2/(V\ s)$ for FTO films deposited via low-temperature sputtering (~170 °C). Similarly, Kam et al.[35] demonstrated that SnO_2 films deposited at room temperature by RF sputtering can achieve μ and N values that make them suitable for use as electron transport layers in optoelectronic devices.

Furthermore, the optical bandgap of the FTO and SnO_2 films is analyzed as a function of oxygen content and

https://doi.org/10.1021/acsaelm.5c01650
ACS Appl. Electron. Mater. 2025, 7, 9489−9504

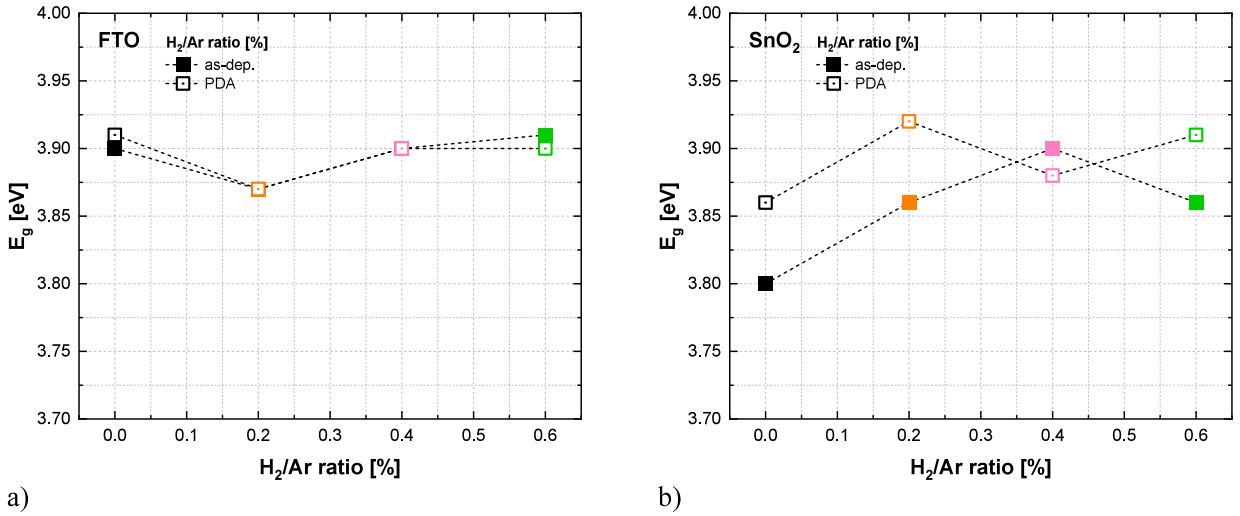

Figure 5. Optical bandgap (E_g) of (a) FTO and (b) SnO_2 films as a function of the H_2/Ar ratio in as deposited (as-dep.) and postdeposition annealed (PDA) states. The oxygen content is fixed at 1% O_2/Ar.

postdeposition annealing in Figure 3. The E_g values are determined from Tauc plots; details are provided in the Supporting Information.

In the FTO films (Figure 3a), the optical bandgap generally exhibits an increasing trend with increasing O_2/Ar ratio in the sputtering atmosphere. The highest values are observed at 0.2% O_2/Ar, reaching 3.92 eV in the as deposited condition and 3.95 eV after PDA. This behavior is consistent with previous reports, where oxygen incorporation during RT sputtering is found to enhance transparency and shift the absorption edge toward higher photon energies.[36]

The SnO_2 films (Figure 3b) exhibit a more stable bandgap across O_2/Ar ratios. The as deposited films show a nearly constant bandgap in the range of 3.76−3.80 eV. After the PDA treatment, the greatest E_g shifts are observed at 0.5% and 0.75% O_2/Ar, with values rising from 3.76 to 3.91 eV. These results are comparable to literature reports of RT sputtered or annealed SnO_2 thin films, where bandgaps in the range of ∼3.7−4.0 eV are commonly observed.[10,37]

In transparent conductive oxides, bandgap widening can result from two opposing effects. The Burstein−Moss shift causes an apparent increase in E_g as conduction band states are filled by free carriers, while bandgap renormalization leads to a slight narrowing due to carrier interactions.[38] However, the Hall measurements of FTO and SnO_2 (Figure 2) generally show a decreasing carrier density with an increasing O_2/Ar ratio. Therefore, the observed bandgap changes are more likely attributed to reduced defect density and improved structural ordering, rather than band-filling effects.

Figure 4 presents the transmittance and reflectance spectra of the samples exhibiting the lowest band-to-band absorption, with films deposited in pure argon being used as the reference. For clarity, only FTO films deposited with 0% and 0.2% O_2/Ar (Figure 4a) and SnO_2 films deposited with 0% and 0.5% O_2/Ar (Figure 4b) are presented. Full T and R spectra for all investigated O_2/Ar ratios are available in the Supporting Information.

The introduction of oxygen into the sputtering gas results in a marked improvement in optical transmittance, as indicated by the red arrow pointing from the pure argon condition toward increasing O_2 content in the gas phase. This enhancement is attributed to reduced sub-bandgap absorption, which shifts the absorption edge toward the ultraviolet region.[39] In contrast, the film sputtered in pure argon exhibits a brownish appearance, consistent with an optical cutoff near 300 nm and more absorptive films.

The fringe shifts in the reflectance spectra of Figure 4a,b likely result from small variations in film thickness rather than changes in the refractive index or density, caused by slight deviations in the deposition rate or uniformity. Although the average reflectance of standalone SnO_2/glass samples remains below 20%, this does not represent device-level behavior. For example, in solar devices in the superstrate configuration, where light enters through the glass substrate before reaching the absorber, reflectance losses are strongly reduced by light-management strategies such as antireflective coatings or textured interfaces.[40]

For the FTO films (Figure 4a), PDA induces only minor changes in both transmittance and reflectance. Meanwhile, the SnO_2 films (Figure 4b) show a more pronounced improvement in transmittance after thermal treatment regardless of the presence of oxygen during deposition.

3.1.2. Hydrogen Series. The hydrogen study is performed at a fixed O_2/Ar ratio of 1%. This approach ensures a consistent and direct comparison between FTO and SnO_2 films, allowing the influence of hydrogen to be isolated from that of oxygen. By maintaining a constant oxygen background, we can more reliably attribute changes in optical and electrical behavior to hydrogen introduced into the sputtering atmosphere. Lower oxygen conditions combined with hydrogen could not be electrically characterized due to sheet resistance values exceeding the measurable range, making 1% O_2/Ar the lowest viable condition for meaningful optoelectrical analysis.

The optical analysis is focused on the evolution of the optical bandgap, as shown in Figure 5. The E_g values are extracted using Tauc plots, as described in Section 2.3, with additional details on the calculation provided in the Supporting Information.

The as deposited FTO films exhibit a narrow bandgap range between 3.87 and 3.91 eV, with PDA inducing only minor changes (Figure 5a). For SnO_2, the optical bandgap widens with increasing H_2/Ar ratio, reaching 3.88 eV at 0.4% H_2/Ar in the as deposited state (Figure 5b). Following thermal treatment, the FTO bandgap undergoes a slight widening,

https://doi.org/10.1021/acsaelm.5c01650
ACS Appl. Electron. Mater. 2025, 7, 9489−9504

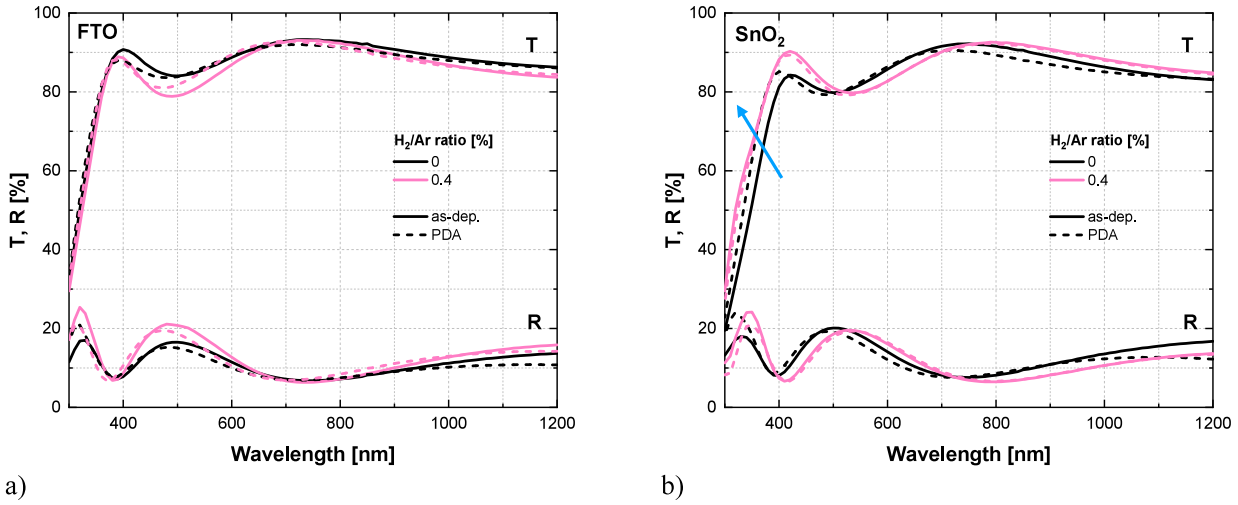

Figure 6. Transmittance (T) and reflectance (R) spectra of (a) FTO and (b) SnO_2 films (~200 nm thick) deposited with 0% and 0.4% H_2/Ar in as deposited (as-dep.) and postdeposition annealed (PDA) states. The oxygen content is fixed at 1% O_2/Ar.

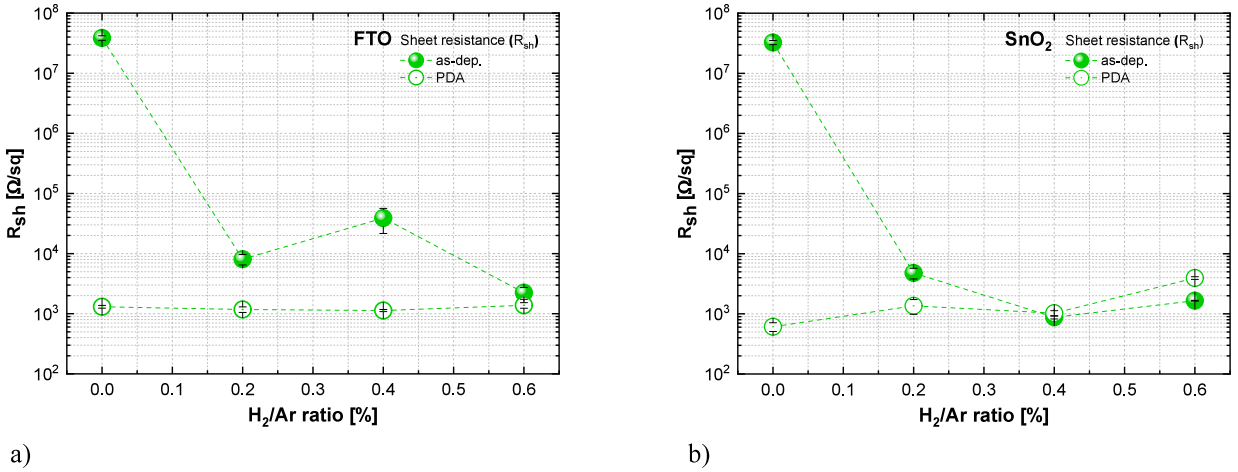

Figure 7. Sheet resistance (R_{sh}) of (a) FTO and (b) SnO_2 films as a function of the H_2/Ar ratio in as deposited (as-dep.) and postdeposition annealed (PDA) conditions. The oxygen content is fixed at 1% O_2/Ar.

peaking at 3.92 eV for 0.2% H_2/Ar. The observed E_g values in hydrogen-containing atmosphere are consistent with previous reports on FTO and SnO_2 films sputtered at room temperature or under low-range thermal conditions (150 °C).[36,41]

Figure 6 presents the transmittance and reflectance spectra for both materials under 0% and 0.4% H_2/Ar conditions. The T and R spectra for other H_2/Ar ratios are provided in the Supporting Information.

In Figure 6a, hydrogen introduction during sputtering leads to a slight decrease in transmittance and a corresponding increase in reflectance, particularly between 400 and 600 nm. Postdeposition annealing induces no significant changes in either trend, indicating a limited optical response to hydrogen in FTO films. This behavior is consistent with previous findings,[42] which show that hydrogen addition to an O_2/Ar sputtering atmosphere does not significantly alter the bandgap energy or optical transparency.

In Figure 6b, the transmittance increases from 0% to 0.4% H_2/Ar, as indicated by the blue arrow. Notably, none of the SnO_2 films deposited in the O_2/Ar atmospheres achieve transmittance values as high as those observed for the 0.4% H_2/Ar sample, which reach an average of approximately 87% across the visible range of the solar spectrum (400−800 nm). However, at higher hydrogen content (0.6% H_2/Ar), a pronounced reduction in transmittance is observed, as shown in the Supporting Information.

Furthermore, hydrogen-containing atmosphere has been reported to influence localized defect states within the bandgap, influencing sub-bandgap absorption.[42] To investigate these defect-related states, the absorption behavior of FTO and SnO_2 films is analyzed by using the Urbach rule (Supporting Information).

For FTO, E_e slightly decreases from 350 (0% H_2/Ar) to 345 meV (0.4% H_2/Ar) in the as deposited state. After annealing, the E_e values converge to 342 meV for both conditions. These results indicate that hydrogen has minimal influence on the sub-bandgap tail states in the FTO films.

For SnO_2, the Urbach energy decreases from 407 (0% H_2/Ar) to 363 meV (0.4% H_2/Ar) in the as deposited state. After PDA, E_e further decreases to 337 meV for the hydrogen-free sample while remaining at 363 meV for the hydrogenated counterpart. This suggests that hydrogen may reduce structural disorder and defect states during deposition. However, hydrogen appears to stabilize shallow defect states and limit further structural relaxation during thermal treatment.

https://doi.org/10.1021/acsaelm.5c01650
ACS Appl. Electron. Mater. 2025, 7, 9489−9504

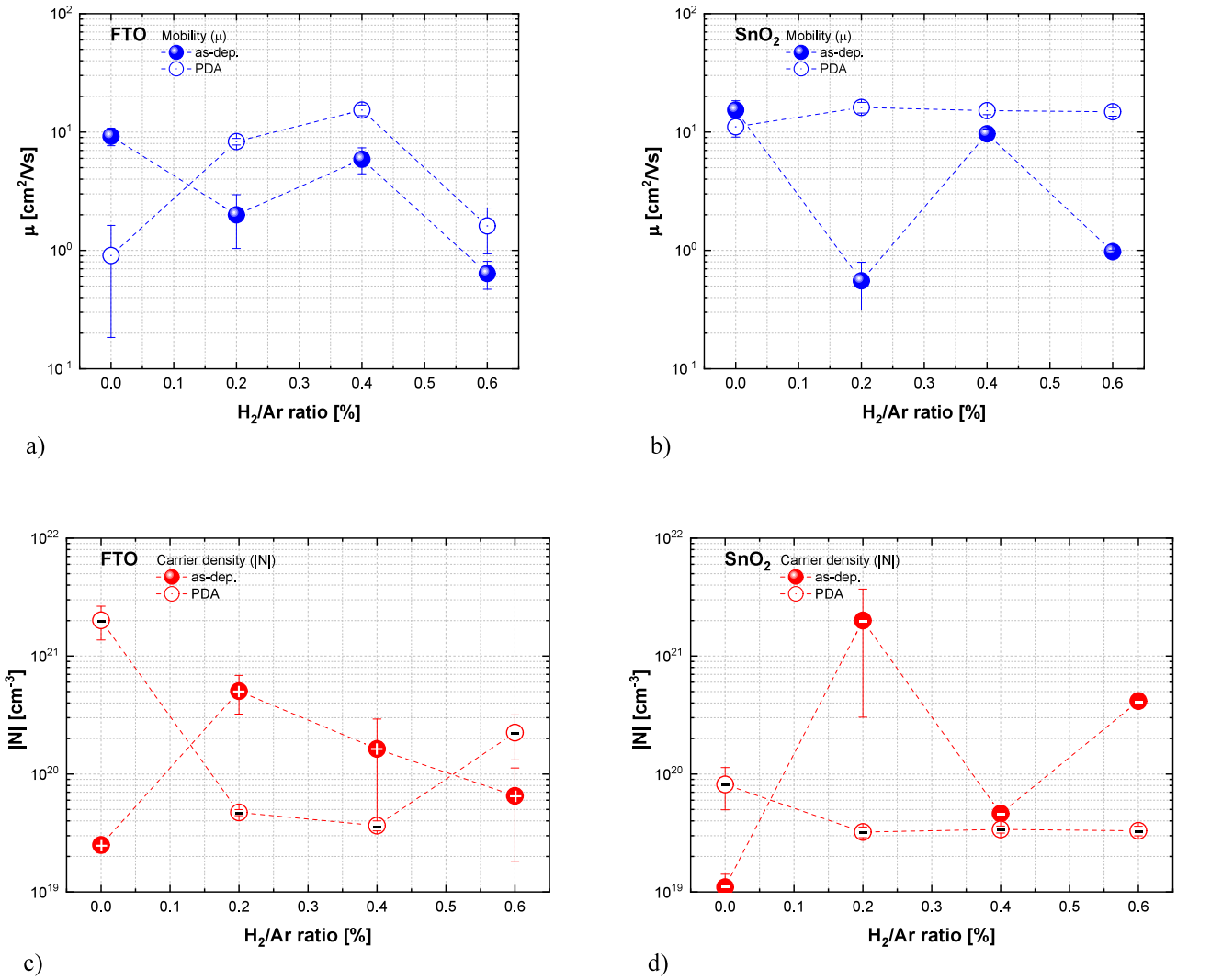

Figure 8. Carrier mobility (μ) and density (N) of (a, c) FTO and (b, d) SnO_2 films as a function of the H_2/Ar ratio in as deposited (as-dep.) and postdeposition annealed (PDA) conditions. The oxygen content is fixed at 1% O_2/Ar. The carrier density sign is reported on the red dots.

Following the analysis of optical properties, the investigation is directed toward the electrical properties of these films. For the as deposited FTO films (Figure 7a), introducing hydrogen into the sputtering atmosphere leads to a reduction in sheet resistance. All samples converge to a value of around 10^3 Ω/sq after PDA. Compared to the pure oxygen series, where the lowest R_{sh} (468 Ω/sq) is achieved at 0.3% O_2/Ar (Figure 1a), the addition of hydrogen does not result in further improvement.

For the SnO_2 films (Figure 7b), the sheet resistance decreases with increasing H_2/Ar ratio in the as deposited condition. After annealing, a significant reduction in R_{sh} is observed at 0% H_2/Ar, indicating that thermal treatment is more effective in enhancing conductivity when no hydrogen is present in the sputtering gas compared to hydrogen-treated samples.

The sheet resistance behavior can be interpreted in light of structural disorder, as quantified by the Urbach energy extracted from the optical analysis. For the FTO films, a slight decrease in Urbach energy with increasing hydrogen content is observed in the as deposited state, accompanied by a significant reduction in R_{sh}. Following PDA, both 0% and 0.4% H_2/Ar samples exhibit similar Urbach energy values, coinciding with stabilized sheet resistance values around 1×10^3 Ω/sq. While this suggests a correlation between reduced structural disorder and improved conductivity, the limited variation in E_e implies that factors beyond the Urbach tail likely dominate the electrical behavior in these films.[43]

For the SnO_2 films, the 0.4% H_2/Ar sample shows lower Urbach energy and sheet resistance than the hydrogen-free sample, indicating reduced disorder and improved conductivity in the as deposited condition. After annealing, E_e and R_{sh} remain nearly unchanged for the hydrogenated sample, while both decrease for the 0% H_2/Ar case.

Therefore, if minimizing sheet resistance is the primary objective, optimized hydrogen content during deposition may eliminate the need for postdeposition annealing, offering a more streamlined and efficient fabrication process for these TCO layers in solar cell devices.

Figure 8 illustrates the evolution of μ and N in the FTO and SnO_2 films as a function of the H_2/Ar ratio under both as deposited and PDA conditions. The carrier density values from the Hall effect reveal both n-type (negative sign) and p-type (positive sign) conduction across FTO and SnO_2 films. A more detailed discussion on this ambipolar behavior is provided in Section 3.1.3, while the Hall measurement procedure is

https://doi.org/10.1021/acsaelm.5c01650
ACS Appl. Electron. Mater. 2025, 7, 9489−9504

described in Section 2.3.1. The corresponding N values for all samples are included in the Supporting Information.

In the FTO samples (Figure 8a,c), the highest mobility of 15.33 $cm^2/(V\ s)$ is observed at 0.4% H_2/Ar after PDA, exceeding the peak value achieved in the oxygen series (13.73 $cm^2/(V\ s)$). The carrier density remains higher in hydrogen-containing atmospheres under both as deposited and annealed conditions compared to the 1% O_2/Ar reference, which reaches 2.5×10^{19} cm^{-3} in the as deposited state.

In Figure 8b,d, both the mobility and carrier density values of the SnO_2 films exhibit noticeable fluctuations in the as deposited state, indicating that hydrogen does not induce a systematic trend in charge transport properties prior to annealing. After PDA, μ and N values stabilize, with mobility peaking at 16.14 $cm^2/(V\ s)$ at 0.4% H_2/Ar and carrier density converging around 3×10^{19} cm^{-3} across all hydrogen-containing conditions.

3.1.3. n-Type and p-Type Conductivity. Both Figure 2 (Section 3.1.1) and Figure 8 (Section 3.1.2) reveal n-type and p-type conduction in the as deposited SnO_2 and FTO films, underscoring the intrinsic ambipolar behavior and complex defect chemistry of undoped or lightly doped metal oxides. This behavior is supported by consistent Hall coefficient signs across repeated measurements of individual samples, while variability in the dominant carrier type between samples reflects the sensitivity of these materials to subtle processing differences. The corresponding average carrier densities and carrier types are provided in the Supporting Information.

This ambipolarity likely arises from native defects, local structural disorder, and the Fermi level's position relative to defect-induced sub-band states. Postdeposition annealing in nitrogen drives all films toward stable n-type behavior, suggesting that a reducing thermal environment promotes electron-donating defects.[44−46]

Previous studies on SnO_x films have demonstrated that even small changes in sputtering conditions can induce abrupt transitions between p- and n-type conduction by modulating oxygen vacancies and tin interstitials. Oxygen-deficient environments tend to favor donor-like defects, facilitating n-type conduction, while slightly oxygen-rich conditions can suppress such donors and promote acceptor-like states, enabling a p-type response.[47] This fine balance between defect types strongly influences the resulting optoelectrical properties.

The observed conduction behavior is consistent with the defect-state model proposed by Henkel et al.,[48] which attributes such phenomena to polaronic states, charge-transfer processes, and excitonic defect configurations. Although a detailed transport mechanism analysis is beyond the scope of this study, the findings underscore the critical role of gas-phase composition during deposition and annealing in shaping the optoelectrical properties and carrier dynamics of SnO_2-based films.

3.1.4. Mobility versus Carrier Density: TCO Overview for Photovoltaics. Figure 9 provides a comparative overview of transparent conducting oxides (TCOs), highlighting the relationship between the carrier mobility and carrier density. All samples, both from this work and the literature, are characterized using the Hall measurement setup described in Sections 2.3 and 2.3.1. The data set includes FTO and SnO_2 films developed in this study, as well as ITO (indium tin oxide), IO:H (hydrogenated indium oxide), AZO (aluminum-doped zinc oxide), and undoped ZnO.

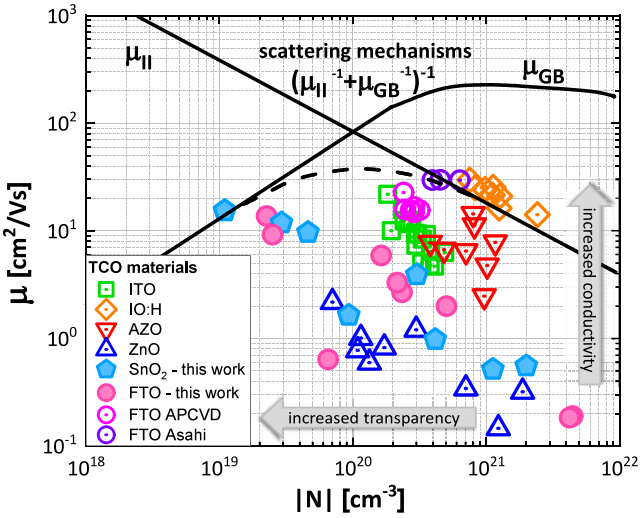

Figure 9. Carrier mobility (μ) as a function of carrier density (N) for various transparent conducting oxides (TCOs). Materials included: fluorine-doped tin oxide (FTO) and undoped SnO_2 deposited in this study by room-temperature RF sputtering; commercial FTO-coated Asahi glass; and FTO deposited by atmospheric pressure chemical vapor deposition (APCVD) at 500 °C. Comparative data for indium tin oxide (ITO), hydrogenated indium oxide (IO:H), aluminum-doped zinc oxide (AZO), and undoped ZnO are included. (Reproduced from ref 49. Available under a CC BY 4.0 license. Copyright 2025 The Authors.) The scattering transport mechanisms, attributed to ionized impurity scattering and grain boundary effects, are indicated by the black lines.

Two high-performance industry benchmarks are also included: commercially available Asahi FTO glass (1.1 mm thick) and FTO deposited via atmospheric pressure chemical vapor deposition (APCVD) at 500 °C,[50] produced in collaboration with the industrial partner of this work. These samples represent the upper performance limits achievable with high-temperature processing.

The plot maps the distribution of TCOs in relation to the two main scattering mechanisms that limit their performance: grain boundary scattering, which dominates at lower carrier densities, and ionized impurity scattering, which becomes significant at higher concentrations.[37,51,52]

The SnO_2 and FTO films fabricated in this work exhibit carrier densities ranging from 10^{19} to over 10^{21} cm^{-3}, with mobilities in the range of 10−15 $cm^2/(V\ s)$. At lower doping levels, the FTO films display mobilities comparable to those of undoped SnO_2, but the absence of significant thermal activation at room temperature limits the extent of dopant activation and crystalline ordering, constraining further mobility improvements.

Additionally, the relatively low carrier density of these films helps suppress free carrier absorption in the near-infrared region, which is beneficial for front electrode applications in solar cells. However, an effective front electrode must also enhance light scattering to increase the optical path length within the absorber layer. The SEM images in the Supporting Information show that the films have smooth and compact surfaces. While this morphology supports efficient charge transport, it does not promote the light scattering needed for an effective front electrode performance.

The APCVD-grown FTO samples show a favorable combination of a $\sim 10^{20}$ cm^{-3} carrier density and higher mobility. This advantage stems from the enhanced crystallinity

https://doi.org/10.1021/acsaelm.5c01650
ACS Appl. Electron. Mater. 2025, 7, 9489−9504

and efficient dopant activation afforded by high-temperature processing (see the Supporting Information). The Asahi FTO reference combines an even higher carrier density with mobility values comparable to those of IO:H.

Although the FTO and SnO_2 films developed here do not match the absolute performance of these high-temperature benchmarks, they demonstrate how room-temperature sputtered TCOs can achieve a balanced optoelectrical performance without the need for thermal processing. However, these gains involve inherent compromises in crystallinity and dopant activation, factors that must be carefully considered when developing low-temperature, scalable deposition strategies for TCOs in photovoltaic applications.

3.2. Material Properties. Reference samples are deposited in four distinct sputtering atmospheres for each material and summarized in Table 1. These representative conditions are chosen to explore the relationship between gas-induced compositional and structural changes and the resulting optoelectrical behavior, discussed in Sections 3.1.1 and 3.1.2.

Table 1. Overview of Sputtering Gas Compositions Used for FTO and SnO_2 Material Characterization[a]

FTO		SnO_2	
O_2/Ar [%]	H_2/Ar [%]	O_2/Ar [%]	H_2/Ar [%]
0	0	0	0
0.4	0	0.5	0
1	0	1	0
1	0.4	1	0.4

[a]The condition labeled as 0% O_2/Ar and 0% H_2/Ar corresponds to sputtering in a pure argon atmosphere.

3.2.1. Energy Dispersive X-ray Spectroscopy Analysis. Energy dispersive X-ray spectroscopy (EDX) is employed to qualitatively and semiquantitatively assess the bulk elemental composition of the deposited FTO and SnO_2 films. Although XPS is later used to probe surface chemistry and oxidation states, EDX complements this by offering information from the bulk region of the films. To minimize interference from parasitic oxygen signals originating from glass substrates, EDX measurements are conducted on samples deposited onto (100)-oriented silicon wafers. This approach ensures a more accurate detection of oxygen and other film-specific elements. Quantitative atomic percentages and measurement uncertainties are provided in the Supporting Information.

Figure 10 shows the EDX spectra of FTO and SnO_2 films deposited in selected sputtering atmospheres. The elemental peaks corresponding to tin (Sn), oxygen (O), and fluorine (F) are clearly detected, consistent with the intended film compositions. A silicon (Si) peak (~1.74 keV) from the silicon substrate is omitted from the displayed spectra for clarity. All spectra are normalized to the O Kα peak (~0.52 keV). Measurements are performed at a 15 kV accelerating voltage.

In both material sets, Sn is consistently observed through its characteristic Nα (~0.39 keV), Mα (~3.44 keV), Mβ (~3.67 keV), and Lα (~3.90 keV) peaks.[53] A weak F Kα peak (~0.68 keV) is identified in the FTO samples. A C Kα peak (~0.28 keV) is also detected and is likely due to surface contamination.

In FTO (Figure 10a), Sn peak intensities are slightly lower for oxygen- and hydrogen-containing atmospheres compared to pure Ar, suggesting a shift toward a more oxidized composition. A modest increase in the fluorine signal is observed under oxygen-rich conditions, potentially indicating improved fluorine incorporation. However, based on EDX results and the comparable optoelectrical behavior between FTO and undoped SnO_2 (Sections 3.1.1 and 3.1.2), fluorine appears to exert limited electronic influence, likely due to the amorphous structure of the films (Section 3.2.3) and the low-temperature deposition environment.[39,54,55]

In SnO_2 films (Figure 10b), Sn peak intensities decrease as the O_2/Ar ratio increases, consistent with increased oxygen uptake. The sample deposited with both O_2 and H_2 shows a slightly elevated Sn signal compared to the O_2-only sample. The presence of hydrogen may reduce the extent of oxygen incorporation, possibly by inducing a mild reducing environment during deposition or promoting the formation of oxygen vacancies.[56]

3.2.2. X-ray Photoelectron Spectroscopy Analysis. X-ray photoelectron spectroscopy (XPS) is performed to analyze the chemical composition and Sn oxidation states in FTO and SnO_2 films under the selected O_2/Ar and H_2/Ar sputtering conditions reported in Table 1.[57] The high-resolution Sn $3d_{5/2}$

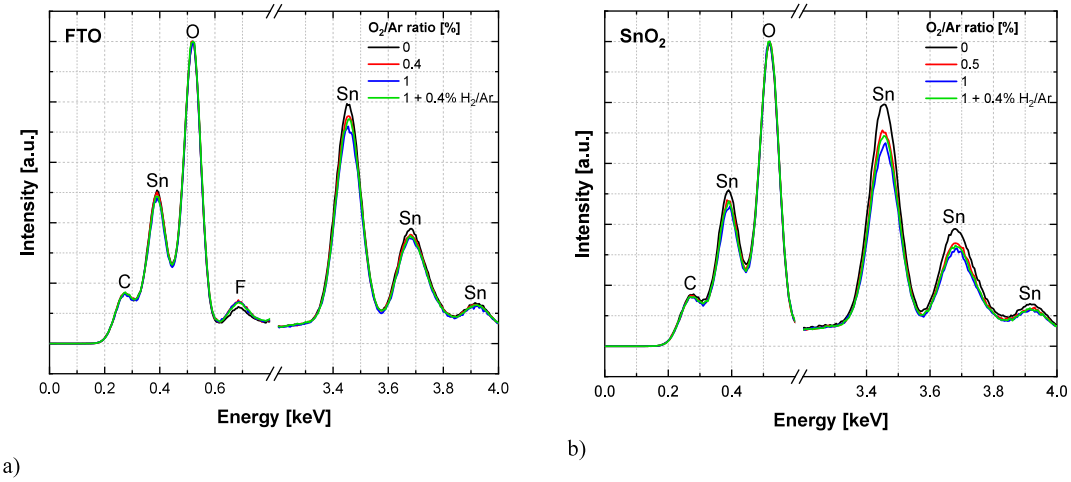

Figure 10. Normalized EDX spectra of (a) FTO and (b) SnO_2 thin films deposited in four distinct sputtering gas atmospheres. Spectra are normalized to the O Kα peak (~0.52 keV). The Sn, O, F, and C peaks are shown and labeled in the spectra.

https://doi.org/10.1021/acsaelm.5c01650
ACS Appl. Electron. Mater. 2025, 7, 9489−9504

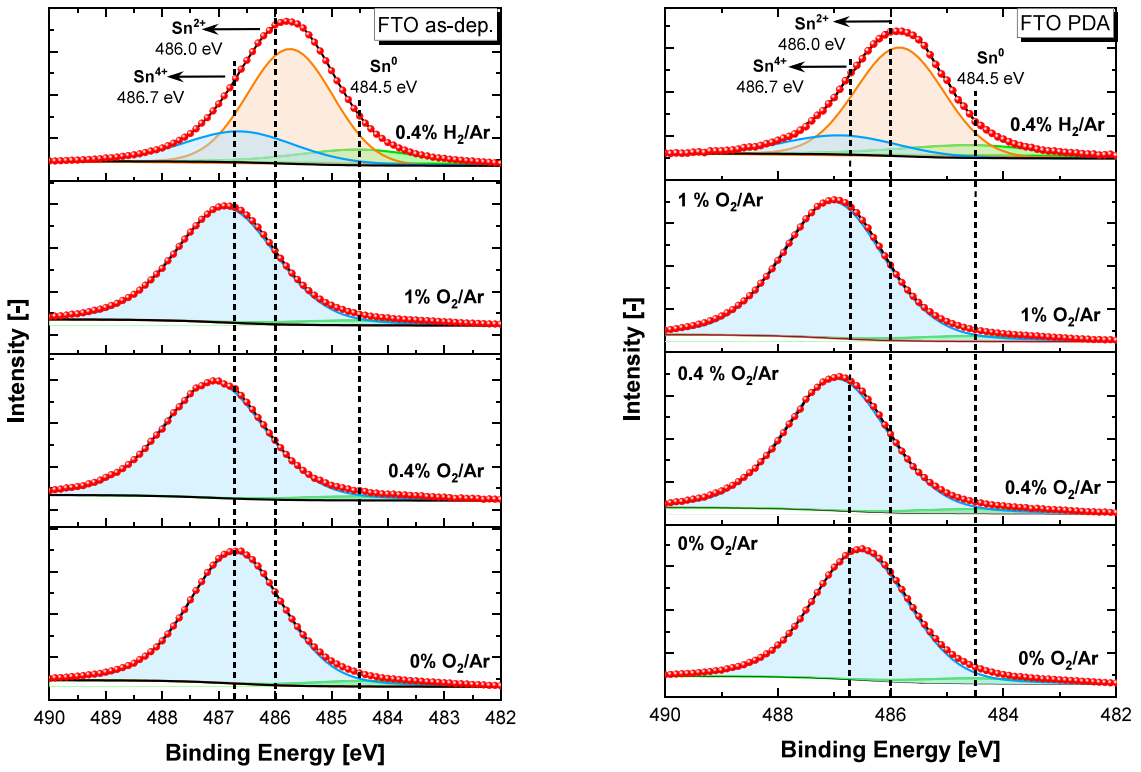

a) b)

Figure 11. XPS spectra in the Sn $3d_{5/2}$ core-level region of FTO films with varied gas ratios in (a) as deposited (as-dep.) and (b) postdeposition annealing (PDA) conditions. The oxygen content is fixed at 1% O_2/Ar for the 0.4% H_2/Ar sample.

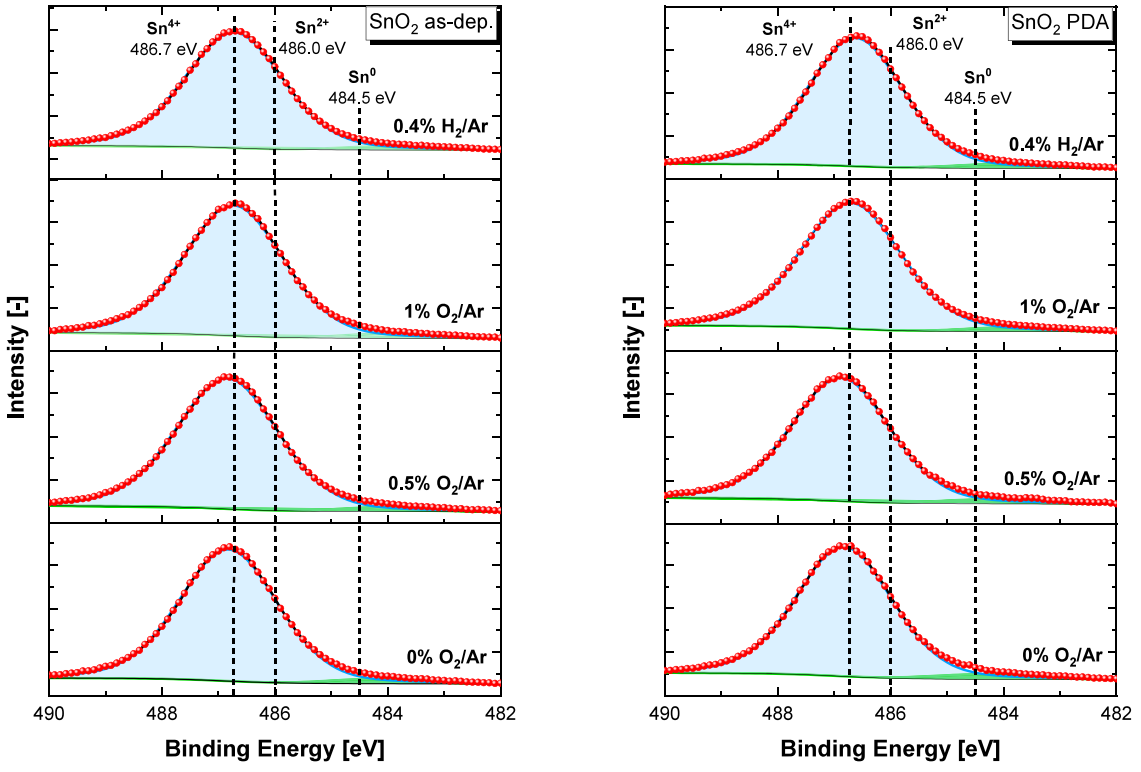

a) b)

Figure 12. XPS spectra in the Sn $3d_{5/2}$ core-level region of SnO_2 films with varied gas ratios in (a) as deposited (as-dep.) and (b) postdeposition annealing (PDA) conditions. The oxygen content is fixed at 1% O_2/Ar for the 0.4% H_2/Ar sample.

https://doi.org/10.1021/acsaelm.5c01650
ACS Appl. Electron. Mater. 2025, 7, 9489−9504

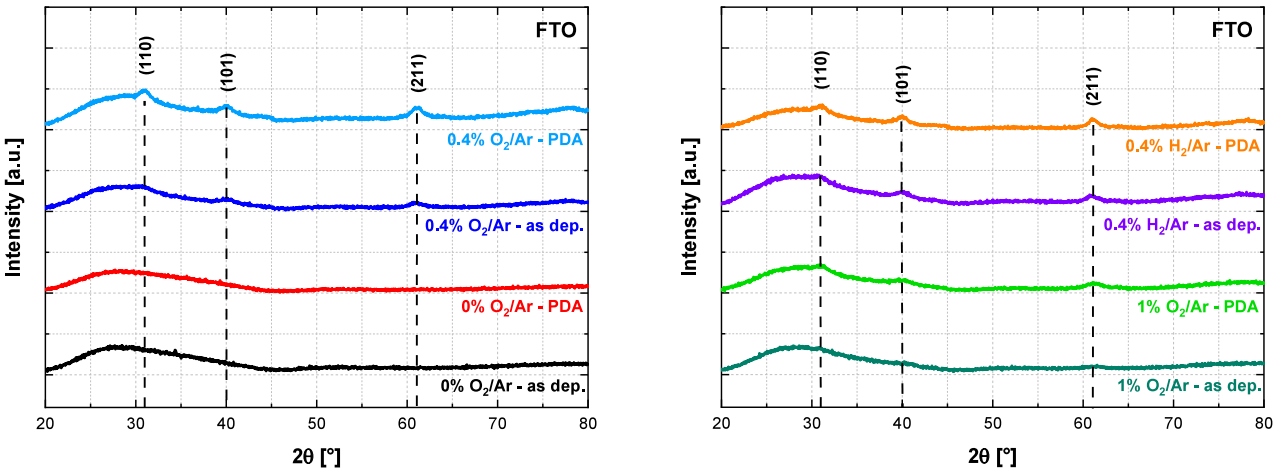

a) b)

Figure 13. XRD patterns of representative FTO films deposited in (a) pure Ar (0% O_2/Ar) and 0.4% O_2/Ar and (b) 1% O_2/Ar and 1% O_2/Ar with 0.4 H_2/Ar, shown for both as deposited (as-dep.) and postdeposition annealed (PDA) conditions.

spectra (Figures 11 and 12) show three components assigned to Sn^0 (484.5 eV), Sn^{2+} (486.0 eV), and Sn^{4+} (486.7 eV), in agreement with literature values.[47,58] The full XPS survey spectra, quantified Sn^0, Sn^{2+}, and Sn^{4+} contents from the high-resolution data, and atomic percentages of all detected elements are provided in the Supporting Information.

In Figure 11, the Sn $3d_{5/2}$ spectra in pure Ar or O_2-containing sputtering atmospheres are dominated by the Sn^{4+} component, indicating a predominantly stoichiometric SnO_2 surface chemistry. In contrast, the spectrum for the 0.4% H_2/Ar sample exhibits a shift toward lower binding energies, with a dominant contribution from suboxidized Sn^{2+} species, indicative of the reducing nature of the sputtering atmosphere.

After annealing, the Sn $3d_{5/2}$ spectra remain largely unchanged across all O_2/Ar compositions, suggesting that the chemical environment at the film surface is stable and not substantially modified by thermal processing. However, in the 0.4% H_2/Ar sample, PDA leads to a notable increase in Sn^{2+} content, with the Sn^{4+} contribution decreasing from 24% to 15% and Sn^{2+} increasing from 62% to 70%. This trend indicates that hydrogen-rich conditions promote substoichiometric tin states. The observed chemical reduction trend is consistent with reports linking increased Sn^{2+} content to the presence of oxygen vacancies in tin oxide systems.[58,59]

The XPS results provide insight into the optoelectrical behavior of the FTO films. While increased O_2/Ar ratios lead to enhanced optical transmittance and bandgap widening (Figures 3a and 4a), they are also accompanied by a significant rise in sheet resistance (Figure 1a). However, these trends cannot be directly linked to changes in Sn oxidation states, as the Sn^{4+} phase remains predominant across all O_2-containing conditions.

In contrast, the enhanced electrical conductivity observed in films sputtered with hydrogen (Figure 7a) may be associated with the presence of Sn^{2+} species, suggesting a correlation with oxygen vacancy formation under reducing conditions. The additional decrease in sheet resistance following PDA further coincides with an increased Sn^{2+} contribution, as revealed by XPS.

Figure 12 presents the high-resolution Sn $3d_{5/2}$ spectra for SnO_2 films deposited under varied gas ratios. Across all conditions, the spectra exhibit a symmetric peak centered near 486.6 eV, characteristic of fully oxidized Sn^{4+} in stoichiometric SnO_2.[55] Postdeposition annealing induces no significant shift in the Sn $3d_{5/2}$ binding energies, reflecting the chemical robustness of the SnO_2 matrix across the investigated conditions. The relative contents of Sn^0, Sn^{2+}, and Sn^{4+} remain largely unchanged before and after annealing, as detailed in the Supporting Information.

In Section 3.1.1, the optoelectrical trends indicate that increasing the O_2/Ar ratio enhances optical transmittance (Figure 4b) but raises sheet resistance (Figure 1b) in the as deposited films. Postdeposition annealing further improves transparency and leads to stabilized conductivity across all gas compositions. However, these variations do not correlate directly with the XPS results, which show minimal shifts in Sn $3d_{5/2}$ binding energy and negligible changes in the relative Sn^0, Sn^{2+}, and Sn^{4+} content.

This discrepancy may be attributed to the surface-sensitive nature of XPS analysis, which probes only the top 5 nm of the film and may not reflect bulk chemical variations. In contrast, the EDX analysis presented in Figure 10b captures the overall stoichiometry of the films and supports the presence of compositional changes not evident from XPS.

In Section 3.1.2, the introduction of hydrogen into an oxygen-rich sputtering atmosphere leads to increased transparency (Figures 5b and 6b) and reduced sheet resistance (Figure 7b), despite no detectable change in the Sn oxidation state. After annealing, the carrier mobility and density values converge across all H_2/Ar conditions. These results suggest that hydrogen may stabilize electronic transport and enhance optoelectrical properties through defect passivation and structural reordering, with no detectable impact on the oxidation state as supported by XPS analysis.[60−62]

3.2.3. X-ray Diffraction Analysis. X-ray diffraction (XRD) is used to assess the structural properties of selected FTO and SnO_2 films deposited at room temperature and annealed at 400 °C for 20 min in a pure nitrogen (N_2) atmosphere. This postdeposition annealing step is intended to promote crystallization in an oxygen-deficient atmosphere.[63]

Due to the limited film thickness (~200 nm), a high background from the amorphous glass substrate is present in the raw patterns. To enhance peak visibility, all spectra have been background-subtracted.

https://doi.org/10.1021/acsaelm.5c01650
ACS Appl. Electron. Mater. 2025, 7, 9489−9504

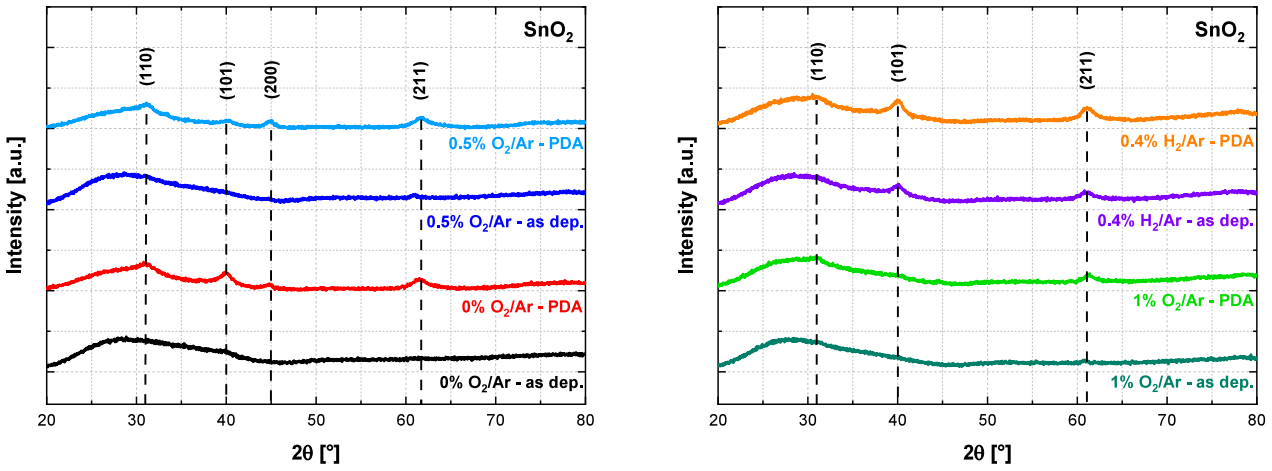

a) b)

Figure 14. XRD patterns of representative SnO_2 films deposited in (a) pure Ar (0% O_2/Ar) and 0.5% O_2/Ar and (b) 1% O_2/Ar and 1% O_2/Ar with 0.4 H_2/Ar, shown for both as deposited (as-dep.) and postdeposition annealed (PDA) conditions.

In FTO films deposited in pure Ar (Figure 13a), no crystalline peaks are observed after PDA, indicating a fully amorphous structure. Oxygen-containing sputtering atmospheres result in weak diffraction features postannealing, corresponding to the (110), (101), and (211) planes of rutile SnO_2. These patterns suggest limited crystallization with no preferred orientation, consistent with randomly oriented nanocrystalline domains.[39]

In Figure 13b, the addition of hydrogen to a 1% O_2/Ar atmosphere slightly enhances crystallization, as evidenced by the sharper and more defined diffraction peaks. However, PDA induces only modest additional changes, suggesting that hydrogen primarily influences early stage grain formation rather than significantly enhancing crystal growth during annealing.[64] In highly disordered or amorphous structures, the lack of well-defined substitutional sites may hinder the effective incorporation of F^- ions, potentially confining them to energetically unfavorable or interstitial positions.[65,66]

These findings suggest that the improved sheet resistance observed after PDA (Figures 1a and 7a) in oxygen-containing sputtering atmospheres, including those with hydrogen, may be linked to the onset of crystallization and the associated structural ordering during the amorphous-to-crystalline transition.

The XRD patterns of SnO_2 films (Figure 14) show generally weak crystallization with no preferred orientation across all tested conditions, consistent with previous reports.[67,68] Postdeposition annealing in nitrogen induces slight structural ordering, although the films remain largely amorphous. Notably, the sample deposited with 1% O_2/Ar and 0.4% H_2 (Figure 14b) shows slightly sharper diffraction peaks compared to the oxygen-only counterpart. As observed in the FTO films, the improvement in sheet resistance after PDA (Figures 1b and 7b) may be associated with the onset of crystallization detected by XRD.

Additionally, the average grain size and full width at half-maximum (fwhm) of the (101) and (211) diffraction peaks are analyzed. fwhm values are corrected for instrumental broadening. The grain sizes are estimated using the Debye−Scherrer equation ($D_{hkl} = 0.9\lambda/(\beta \cos \theta)$), where D_{hkl} is the grain size, λ is wavelength of Cu Kα radiation (λ = 0.15406 nm), β is the fwhm value in the radian scale, and θ is the Bragg diffraction angle.[69] The resulting grain sizes range from 6.8 to 9 nm for FTO films and from 6.5 to 7.5 nm for SnO_2 films.

While fluorine incorporation at elevated temperatures (e.g., ≥400 °C) is known to promote crystallite growth,[70] the consistently small grain sizes and weak diffraction peaks observed in fluorine-containing films here suggest that fluorine primarily aids nucleation without significantly enhancing grain growth under RT conditions. Crystallite sizes remain in the nanometer range, indicating that the thermal energy available during RT sputtering is insufficient to drive significant structural coarsening.

4. CONCLUSIONS

This study systematically investigates the impact of reactive sputtering gas composition on the optoelectrical, structural, and surface chemical properties of room-temperature (RT) sputtered fluorine-doped tin oxide (FTO) and undoped tin dioxide (SnO_2) thin films. By correlating optical transmittance, charge transport, sheet resistance, and spectroscopic data, critical processing−property relationships are identified to guide the design of these transparent conducting oxides (TCOs) for photovoltaic applications. The results demonstrate competitive optoelectrical properties compared to typical RT sputtered SnO_2-based films, highlighting that careful control of the sputtering gas composition can effectively tune and improve film performance.

First, oxygen incorporation in the sputtering atmosphere governs the balance between the optical transparency and electrical conductivity. In FTO, 0.3−0.4% O_2/Ar ratios yield the lowest sheet resistance (468 Ω/sq) and highest carrier mobility (13.7 $cm^2/(V\ s)$) while maintaining a wide optical bandgap (E_g > 3.9 eV). In undoped SnO_2, sheet resistance increases monotonically with oxygen content. However, the optimum condition occurs at 1% O_2/Ar, where mobility peaks (15.3 $cm^2/(V\ s)$) with moderate carrier density (~10^{19} cm^{-3}).

Second, introducing hydrogen into an oxygen-rich atmosphere (1% O_2/Ar) significantly influences the optoelectrical response of undoped SnO_2 films. Hydrogen addition enhances transparency and reduces sheet resistance in the as deposited state. XPS analysis shows no change in the dominant Sn^{4+} oxidation state, suggesting that hydrogen acts primarily through defect passivation and structural modification rather

https://doi.org/10.1021/acsaelm.5c01650
ACS Appl. Electron. Mater. 2025, 7, 9489−9504

than chemical reduction. After postdeposition annealing (PDA) at 400 °C in N_2 atmosphere, both hydrogenated and nonhydrogenated samples exhibit converging mobilities and carrier densities. In FTO films, hydrogen has a subtle effect on optical properties, while conductivity stabilizes at $\sim 10^3$ Ω/sq after PDA.

Although RT sputtered FTO and SnO_2 films do not yet match the optoelectrical performance achieved by high-temperature deposition methods, precise control over the sputtering gas composition enables a tunable balance between the transparency and conductivity. This provides a thermally compatible, scalable, and cost-effective strategy for fabricating transparent conductive electrodes and charge transport layers particularly suited for thermally sensitive technologies such as polymer-based and next-generation solar cells.

■ ASSOCIATED CONTENT

Supporting Information

The Supporting Information is available free of charge at https://pubs.acs.org/doi/10.1021/acsaelm.5c01650.

Extended reflectance and transmittance spectra; Tauc plot analysis; Urbach energy study for hydrogen series; carrier type and density data; EDX data; extended XPS data; XRD analysis of high-temperature APCVD FTO sample; and SEM analysis (PDF)

■ AUTHOR INFORMATION

Corresponding Author

Federica Saitta − *Photovoltaic Materials and Devices group, Delft University of Technology, 2628 CD Delft, The Netherlands;* orcid.org/0009-0004-2120-2223; Email: f.s.saitta@tudelft.nl

Authors

Govind Padmakumar − *Photovoltaic Materials and Devices group, Delft University of Technology, 2628 CD Delft, The Netherlands*

Paula Perez Rodriguez − *Photovoltaic Materials and Devices group, Delft University of Technology, 2628 CD Delft, The Netherlands*

Alestair Wilson − *Photovoltaic Materials and Devices group, Delft University of Technology, 2628 CD Delft, The Netherlands*

Prasad Gonugunta − *Department of Materials Science and Engineering, Delft University of Technology, Faculty of Mechanical Engineering (ME), 2628 CD Delft, The Netherlands*

Prasaanth Ravi Anusuyadevi − *Department of Materials Science and Engineering, Delft University of Technology, Faculty of Mechanical Engineering (ME), 2628 CD Delft, The Netherlands*

Rudi Santbergen − *Photovoltaic Materials and Devices group, Delft University of Technology, 2628 CD Delft, The Netherlands*

Arno H.M. Smets − *Photovoltaic Materials and Devices group, Delft University of Technology, 2628 CD Delft, The Netherlands*

Complete contact information is available at: https://pubs.acs.org/10.1021/acsaelm.5c01650

Author Contributions

The manuscript was written through contributions of all authors. All authors have given approval to the final version of the manuscript.

Funding

Financial support was provided by HyET Solar Netherlands B.V.

Notes

The authors declare no competing financial interest.

■ ACKNOWLEDGMENTS

The Photovoltaic Materials and Devices (PVMD) group of the Electrical Sustainable Energy Department at Delft University of Technology is gratefully acknowledged for its support. Special thanks are extended to Dhr. Ruud Hendrikx from the Department of Materials Science and Engineering at Delft University of Technology for conducting the X-ray analysis. Additionally, appreciation is given to the bilateral collaboration between HyET Solar and Delft University of Technology, whose funding and support were essential in advancing this research.

■ REFERENCES

(1) Ramarajan, R.; Paul Joseph, D.; Thangaraju, K.; Kovendhan, M. Indium-Free Alternative Transparent Conducting Electrodes: An Overview and Recent Developments. *Environmental Chemistry for a Sustainable World* **2021**, *55*, 149−183.

(2) Koida, T.; Nomoto, J. Sustainable Transparent Conducting Oxides: Insights from Amorphous SnOx Thin Films via Oxygen Stoichiometry Control. *Chem. Mater.* **2024**, *36* (14), 6838−6848.

(3) Cao, H.; Liang, L. Tin Oxide-Based Thin-Film Transistors and Their Circuits. In *Tin Oxide Materials*; Elsevier, 2020; pp 441−476. DOI: 10.1016/B978-0-12-815924-8.00015-3.

(4) Suh, S.; Zhang, Z.; Chu, W. K.; Hoffman, D. M. Atmospheric-Pressure Chemical Vapor Deposition of Fluorine-Doped Tin Oxide Thin Films. *Thin Solid Films* **1999**, *345* (2), 240−243.

(5) Dalapati, G. K.; Sharma, H.; Guchhait, A.; Chakrabarty, N.; Bamola, P.; Liu, Q.; Saianand, G.; Sai Krishna, A. M.; Mukhopadhyay, S.; Dey, A.; Wong, T. K. S.; Zhuk, S.; Ghosh, S.; Chakrabortty, S.; Mahata, C.; Biring, S.; Kumar, A.; Ribeiro, C. S.; Ramakrishna, S.; Chakraborty, A. K.; Krishnamurthy, S.; Sonar, P.; Sharma, M. Tin Oxide for Optoelectronic, Photovoltaic and Energy Storage Devices: A Review. *J. Mater. Chem. A* **2021**, *9* (31), 16621−16684.

(6) Yu, C.; Zou, Q.; Wang, Q.; Zhao, Y.; Ran, X.; Dong, G.; Peng, C.-W.; Allen, V.; Cao, X.; Zhou, J.; Zhao, Y.; Zhang, X. Silicon Solar Cell with Undoped Tin Oxide Transparent Electrode. *Nat. Energy* **2023**, *8* (10), 1119−1125.

(7) Mussabekova, A. K.; Ilyassov, B. R.; Aimukhanov, A. K.; Tussupbekova, A. K.; Zeinidenov, A. K.; Valiev, D.; Paygin, V.; Kudryashov, V. V.; Zhakanova, A. M. Promising SnO_x Electron Transport Layer for Polymer Solar Cells. *Physica B* **2023**, *666*, 415113.

(8) Muthukumar, A.; Giusti, G.; Jouvert, M.; Consonni, V.; Bellet, D. Fluorine-Doped SnO_2 Thin Films Deposited on Polymer Substrate for Flexible Transparent Electrodes. *Thin Solid Films* **2013**, *545*, 302−309.

(9) Tao, H.; Ma, Z.; Yang, G.; Wang, H.; Long, H.; Zhao, H.; Qin, P.; Fang, G. Room-Temperature Processed Tin Oxide Thin Film as Effective Hole Blocking Layer for Planar Perovskite Solar Cells. *Appl. Surf. Sci.* **2018**, *434*, 1336−1343.

(10) Qiu, L.; Liu, Z.; Ono, L. K.; Jiang, Y.; Son, D.-Y.; Hawash, Z.; He, S.; Qi, Y. Scalable Fabrication of Stable High-Efficiency Perovskite Solar Cells and Modules Utilizing Room-Temperature Sputtered SnO_2 Electron Transport Layer. *Adv. Funct. Mater.* **2019**, *29* (47), 1806779.

(11) Palmstrom, A. F.; Eperon, G. E.; Leijtens, T.; Prasanna, R.; Habisreutinger, S. N.; Nemeth, W.; Gaulding, E. A.; Dunfield, S. P.; Reese, M.; Nanayakkara, S.; Moot, T.; Werner, J.; Liu, J.; To, B.; Christensen, S. T.; McGehee, M. D.; van Hest, M. F. A. M.; Luther, J. M.; Berry, J. J.; Moore, D. T. Enabling Flexible All-Perovskite Tandem Solar Cells. *Joule* **2019**, *3* (9), 2193−2204.
(12) Koida, T.; Matsui, T.; Sai, H. Amorphous SnO_2 as Earth-Abundant Stable Transparent Conductive Oxide and Its Application to Si Heterojunction Solar Cells. *Sol. RRL* **2023**, *7* (18), 2300381.
(13) Sai, H.; Koida, T.; Matsui, T. Improved Electrical Contact Properties in Indium-Free Silicon Heterojunction Solar Cells with Amorphous SnO_2 TCO Layers. *Sol. Energy Mater. Sol. Cells* **2024**, *278*, 113191.
(14) Sahli, F.; Werner, J.; Kamino, B. A.; Bräuninger, M.; Monnard, R.; Paviet-Salomon, B.; Barraud, L.; Ding, L.; Diaz Leon, J. J.; Sacchetto, D.; Cattaneo, G.; Despeisse, M.; Boccard, M.; Nicolay, S.; Jeangros, Q.; Niesen, B.; Ballif, C. Fully Textured Monolithic Perovskite/Silicon Tandem Solar Cells with 25.2% Power Conversion Efficiency. *Nat. Mater.* **2018**, *17* (9), 820−826.
(15) Zarrinkhameh, M.; Zendehnam, A.; Hosseini, S. M.; Robatmili, N.; Arabzadegan, M. Effect of Oxidation and Annealing Temperature on Optical and Structural Properties of SnO_2. *Bull. Mater. Sci.* **2014**, *37* (3), 533−539.
(16) Baco, S.; Chik, A.; Yassin, F. M. Study on Optical Properties of Tin Oxide Thin Film at Different Annealing Temperature. *Journal of Science and Technology* **2012**, *4* (1), 1.
(17) Chen, Q. Z.; Zhang, Z. X.; Fu, W. Q.; Duan, J. R.; Yang, Y. X.; Chen, C. N.; Lien, S. Y. Low Resistivity and High Carrier Concentration in SnO_2 Thin Films: The Impact of Nitrogen−Hydrogen Annealing Treatments. *Nanomaterials* **2025**, *15* (13), 986.
(18) Yates, H. M.; Evans, P.; Sheel, D. W.; Nicolay, S.; Ding, L.; Ballif, C. The Development of High Performance SnO_2:F as TCOs for Thin Film Silicon Solar Cells. *Surf. Coat. Technol.* **2012**, *213*, 167−174.
(19) Wang, Y.; Ba, Z.; Dong, S.; Xie, W.; Wu, Z.; Ran, C. Advancing SnO_2 Electron Transport Layer for Efficient Perovskite Photovoltaics: A Critical Review. *ACS Appl. Mater. Interfaces* **2025**, *17* (19), 27651−27670.
(20) Uddin, A.; Yi, H. Progress and Challenges of SnO_2 Electron Transport Layer for Perovskite Solar Cells: A Critical Review. *Sol. RRL* **2022**, *6* (6), 2100983.
(21) Hernandez-Gutierrez, C. A.; Vigil Galan, O.; Melo, S.; Rodriguez, E.; Kudriavtsev, Y. The Role of SnO_2 High Resistivity Transparent Layer Deposited onto Commercial Conducting Glass as Front Contact in Superstrate Configuration Thin Film Solar Cells Technology: Influence of the Deposition Technique. *Rev. Mex. Fis.* **2019**, *65* (5), 554−559.
(22) Guillén, C. Determination of the Band Gap Energy of SnO_2 and ZnO Thin Films with Different Crystalline Qualities and Doping Levels. *Electron. Mater.* **2025**, *6* (1), 3.
(23) Riungu, G. G.; Mugo, S. W.; Ngaruiya, J. M.; John, G. M.; Mugambi, N. Optical Band Energy, Urbach Energy and Associated Band Tails of Nanocrystalline TiO_2 Films at Different Annealing Rates. *Am. J. Nanosciences* **2021**, *7* (1), 28−34.
(24) Bakr, N. A.; Salman, S. A.; Ali, M. N. Effect of Fluorine Doping on Structural and Optical Properties of SnO_2 Thin Films Prepared by Chemical Spray Pyrolysis Method. *Adv. Mater.* **2016**, *5* (4), 23−30.
(25) Ikhmayies, S. J.; Ahmad-Bitar, R. N. An Investigation of the Bandgap and Urbach Tail of Spray-Deposited SnO_2:F Thin Films. *Phys. Scr.* **2011**, *84* (5), 055801.
(26) Ponte, R.; Rauwel, E.; Rauwel, P. Tailoring SnO_2 Defect States and Structure: Reviewing Bottom-Up Approaches to Control Size, Morphology, Electronic and Electrochemical Properties for Application in Batteries. *Materials* **2023**, *16* (12), 4339.
(27) Batal, M.A.; Nashed, G.; Jneed, F. H. Conductivity and Thermoelectric Properties of Nanostructure Tin Oxide Thin Films. *J. Assoc. Arab Univ. Basic Appl. Sci.* **2014**, *15*, 15−20.
(28) Jain, S. H.; Griffin, P. B.; Plummer, J. D. Hall Measurements of Bilayer Structures. *J. Appl. Phys.* **2003**, *93* (2), 1060−1063.
(29) Wali, Q.; Aamir, M.; Ejaz Khan, M.; Jose, R.; Fan, W.; Yang, S. Tin Oxide as an Electron Transport Layer in Perovskite Solar Cells: Advances and Challenges. *Sol. Energy* **2024**, *270*, 112382.
(30) Xiong, L.; Guo, Y.; Wen, J.; Liu, H.; Yang, G.; Qin, P.; Fang, G. Review on the Application of SnO_2 in Perovskite Solar Cells. *Adv. Funct. Mater.* **2018**, *28* (35), 1802757.
(31) Peelaers, H.; Kioupakis, E.; Van de Walle, C. G. Fundamental Limits on Optical Transparency of Transparent Conducting Oxides: Free-Carrier Absorption in SnO_2. *Appl. Phys. Lett.* **2012**, *100* (1), 011914.
(32) Miccoli, I.; Edler, F.; Pfnür, H.; Tegenkamp, C. The 100th Anniversary of the Four-Point Probe Technique: The Role of Probe Geometries in Isotropic and Anisotropic Systems. *J. Phys.: Condens. Matter* **2015**, *27* (22), 223201.
(33) Orton, J. W.; Powell, M. J. The Hall Effect in Polycrystalline and Powdered Semiconductors. *Rep. Prog. Phys.* **1980**, *43* (11), 1263.
(34) Zheng, W.; Zhang, Y. N.; Tian, J. Q. Effect of Fluorine Doping Concentration on Semiconductive Property of Tin Dioxide. *Chalcogenide Lett.* **2017**, *14* (7), 275−281.
(35) Kam, M.; Zhang, Q.; Zhang, D.; Fan, Z. Room-Temperature Sputtered SnO_2 as Robust Electron Transport Layer for Air-Stable and Efficient Perovskite Solar Cells on Rigid and Flexible Substrates. *Sci. Rep.* **2019**, *9* (1), 6963.
(36) Morán-Pedroso, M.; Sánchez-Marcos, J.; de Andrés, A.; Prieto, C. Fluorinated Tin Oxide (FTO) Deposited at Room Temperature: Influence of Hydrogen and Oxygen in the Sputtering Gas on the Optical and Electrical Properties. *Appl. Surf. Sci.* **2018**, *459*, 349−353.
(37) Kim, I. H.; Ko, J. H.; Kim, D.; Lee, K. S.; Lee, T. S.; Jeong, J.-H.; Cheong, B.; Baik, Y.-J.; Kim, W. M. Scattering Mechanism of Transparent Conducting Tin Oxide Films Prepared by Magnetron Sputtering. *Thin Solid Films* **2006**, *515* (4), 2475−2480.
(38) Saw, K. G.; Aznan, N. M.; Yam, F. K.; Ng, S. S.; Pung, S. Y. New Insights on the Burstein-Moss Shift and Band Gap Narrowing in Indium-Doped Zinc Oxide Thin Films. *PLoS One* **2015**, *10* (10), No. e0141180.
(39) Banyamin, Z. Y.; Kelly, P. J.; West, G.; Boardman, J. Electrical and Optical Properties of Fluorine Doped Tin Oxide Thin Films Prepared by Magnetron Sputtering. *Coatings* **2014**, *4* (4), 732−746.
(40) Haug, F. J.; Ballif, C. Light Management in Thin Film Silicon Solar Cells. *Energy Environ. Sci.* **2015**, *8* (3), 824−837.
(41) Zhu, B. L.; Liu, F.; Li, K.; Lv, K.; Wu, J.; Gan, Z. H.; Liu, J.; Zeng, D. W.; Xie, C. S. Sputtering Deposition of Transparent Conductive F-Doped SnO_2 (FTO) Thin Films in Hydrogen-Containing Atmosphere. *Ceram. Int.* **2017**, *43* (13), 10288−10298.
(42) Morán-Pedroso, M.; Gago, R.; Julin, J.; Salas-Colera, E.; Jimenez, I.; De Andrés, A.; Prieto, C. Correlated Effects of Fluorine and Hydrogen in Fluorinated Tin Oxide (FTO) Transparent Electrodes Deposited by Sputtering at Room Temperature. *Appl. Surf. Sci.* **2021**, *537*, 147906.
(43) Rahal, A.; Benramache, S.; Benhaoua, B. The Effect of the Film Thickness and Doping Content of SnO_2:F Thin Films Prepared by the Ultrasonic Spray Method. *J. Semicond.* **2013**, *34* (9), 093003.
(44) Schleife, A.; Varley, J. B.; Fuchs, F.; Rödl, C.; Bechstedt, F.; Rinke, P.; Janotti, A.; Van de Walle, C. G. Tin Dioxide from First Principles: Quasiparticle Electronic States and Optical Properties. *Phys. Rev. B* **2011**, *83* (3), 035116.
(45) Ni, Z.; Yu, Z.; Huang, J. Unveiling the Ambipolar Carrier Transport Property of SnO_{2-x} for Multiple-Functional Interlayers in Perovskite Solar Cells. *Appl. Phys. Lett.* **2021**, *119* (12), 123501 DOI: 10.1063/5.0066843.
(46) Herklotz, F.; Lavrov, E. V.; Melnikov, V. V.; Galazka, Z.; Agekyan, V. F. Comprehensive Study of the Interstitial Hydrogen Donor in SnO_2. *Phys. Rev. B* **2023**, *108* (20), 205204.
(47) Luo, H.; Liang, L. Y.; Cao, H. T.; Liu, Z. M.; Zhuge, F. Structural, Chemical, Optical, and Electrical Evolution of SnO_x Films Deposited by Reactive RF Magnetron Sputtering. *ACS Appl. Mater. Interfaces* **2012**, *4* (10), 5673−5677.
(48) Henkel, K.; Haeberle, J.; Müller, K.; Janowitz, C.; Schmeißer, D. Preparation, Properties and Electronic Structure of SnO_2. In *Single*

Crystals of Electronic Materials; Woodhead Publishing, 2019; pp 547−572. DOI: 10.1016/B978-0-08-102096-8.00016-1.
(49) Saitta, F.; Kalpoe, P.; Ahluwalia, V.; Padmakumar, G.; Rodriguez, P. P.; Limodio, G.; Santbergen, R.; Smets, A. H.M. De-Coupling of Optical and Electrical Properties in Front TCO Using the Bilayer Concept for Thin-Film Solar Cells. *Sol. Energy Mater. Sol. Cells* **2025**, *290*, 113723.
(50) Venkataraman, S. Investigation of Opto-Electrical and Structural Properties of Atmospheric Pressure Chemical Vapor Deposition of Fluorine-Doped Tin Oxide. Master's Thesis, Delft University of Technology, 2023. https://resolver.tudelft.nl/uuid:13168b29-6290-4166-bea2-8200b34edf79.
(51) Zhang, D. H.; Ma, H. L. Scattering Mechanisms of Charge Carriers in Transparent Conducting Oxide Films. *Appl. Phys. A: Mater. Sci. Process.* **1996**, *62* (5), 487−492.
(52) Minami, T. New N-Type Transparent Conducting Oxides. *MRS Bull.* **2000**, *25* (8), 38−44.
(53) Rahman, M. T.; Ahmed, Z.; Islam, M. J.; Kamaruzzaman; Khatun, M. T.; Gafur, M. A.; Bashar, M. S.; Alam, M. M. Comparative Study of Structural, Optical and Electrical Properties of SnO_2 Thin Film Growth via CBD, Drop-Cast and Dip-Coating Methods. *Mater. Sci. Appl.* **2021**, *12* (12), 578−594.
(54) Elangovan, E.; Singh, M. P.; Ramamurthi, K. Studies on Structural and Electrical Properties of Spray Deposited SnO_2:F Thin Films as a Function of Film Thickness. *Mater. Sci. Eng., B* **2004**, *113* (2), 143−148.
(55) Batzill, M.; Diebold, U. The Surface and Materials Science of Tin Oxide. *Prog. Surf. Sci.* **2005**, *79* (2−4), 47−154.
(56) Ali, F.; Pham, N. D.; Bradford, H. J.; Khoshsirat, N.; Ostrikov, K.; Bell, J. M.; Wang, H.; Tesfamichael, T. Tuning the Amount of Oxygen Vacancies in Sputter-Deposited SnO_x Films for Enhancing the Performance of Perovskite Solar Cells. *ChemSusChem* **2018**, *11* (18), 3096−3103.
(57) Szuber, J.; Czempik, G.; Larciprete, R.; Koziej, D.; Adamowicz, B. XPS Study of the L-CVD Deposited SnO_2 Thin Films Exposed to Oxygen and Hydrogen. *Thin Solid Films* **2001**, *391* (2), 198−203.
(58) Hsu, P. C.; Hsu, C. J.; Chang, C. H.; Tsai, S. P.; Chen, W. C.; Hsieh, H. H.; Wu, C. C. Sputtering Deposition of P-Type SnO Films with SnO_2 Target in Hydrogen-Containing Atmosphere. *ACS Appl. Mater. Interfaces* **2014**, *6* (16), 13724−13729.
(59) Hsu, P. C.; Tsai, S. P.; Chang, C. H.; Hsu, C. J.; Chen, W. C.; Hsieh, H. H.; Wu, C. C. Preparation of P-Type SnO Thin Films and Transistors by Sputtering with Robust Sn/SnO_2 Mixed Target in Hydrogen-Containing Atmosphere. *Thin Solid Films* **2015**, *585*, 50−56.
(60) Minami, T. Transparent Conducting Oxide Semiconductors for Transparent Electrodes. *Semicond. Sci. Technol.* **2005**, *20* (4), S35.
(61) Flak, D.; Braun, A.; Mun, B. S.; Park, J. B.; Parlinska-Wojtan, M.; Graule, T.; Rekas, M. Spectroscopic Assessment of the Role of Hydrogen in Surface Defects, in the Electronic Structure and Transport Properties of TiO_2, ZnO and SnO_2 Nanoparticles. *Phys. Chem. Chem. Phys.* **2013**, *15* (5), 1417−1431.
(62) Borges, P. D.; Scolfaro, L.; Assali, L. V. C. Complex Centers of Hydrogen in Tin Dioxide. *Theor. Chem. Acc.* **2015**, *134* (11), 131.
(63) Abdullahi, S; Sani, F.; Idris, A. T.; Aliyu, M. W.; Abdullahi, B. Structural and Electrical Properties of Fluorine Doped Tin Oxide (FTO) Thin Film Deposited by Spin Coating Technique. *Int. J. Sci. Glob. Sustain.* **2024**, *10* (3), 69−76.
(64) Martínez-Puente, M. A.; Tirado, J.; Jaramillo, F.; Garza-Hernández, R.; Horley, P.; Silva Vidaurri, L. G.; Aguirre-Tostado, F. S.; Martínez-Guerra, E. Unintentional Hydrogen Incorporation into the SnO_2 Electron Transport Layer by ALD and Its Effect on the Electronic Band Structure. *ACS Appl. Energy Mater.* **2021**, *4* (10), 10896−10908.
(65) Wang, X.; Wang, X.; Di, Q.; Zhao, H.; Liang, B.; Yang, J. Mutual Effects of Fluorine Dopant and Oxygen Vacancies on Structural and Luminescence Characteristics of F-Doped SnO_2 Nanoparticles. *Materials* **2017**, *10* (12), 1398.
(66) Adjimi, A.; Zeggar, M. L.; Attaf, N.; Aida, M. S. Fluorine-Doped Tin Oxide Thin Films Deposition by Sol-Gel Technique. *J. Crystallization Process Technol.* **2018**, *08* (04), 89−106.
(67) Tosun, B. S.; Feist, R. K.; Gunawan, A.; Mkhoyan, K. A.; Campbell, S. A.; Aydil, E. S. Sputter Deposition of Semicrystalline Tin Dioxide Films. *Thin Solid Films* **2012**, *520* (7), 2554−2561.
(68) Yang, Y.; Maeng, B.; Jung, D. G.; Lee, J.; Kim, Y.; Kwon, J.; An, H. K.; Jung, D. Annealing Effects on SnO_2 Thin Film for H_2 Gas Sensing. *Nanomaterials* **2022**, *12* (18), 3227.
(69) Kim, N. H.; Kim, H. K.; Lee, K. M.; Sohn, H. C.; Roh, J. S.; Choi, D. J. Effects of Ag Doping on the Crystallization Properties of Sb-Rich GeSb Thin Films. *Thin Solid Films* **2011**, *519* (16), 5323−5328.
(70) Elsherif, O. S.; Muftah, G. E. A.; Abubaker, O.; Dharmadasa, I. M. Structural, Optical and Electrical Properties of SnO_2:F Thin Films Deposited by Spray Pyrolysis for Application in Thin Film Solar Cells. *J. Mater. Sci.: Mater. Electron.* **2016**, *27* (12), 12280−12286.

https://doi.org/10.1021/acsaelm.5c01650
ACS Appl. Electron. Mater. 2025, 7, 9489−9504